



Universiteit Utrecht



Netherlands Institute for Space Research

Opleiding Natuur- en Sterrenkunde Opleiding Scheikunde

Investigating the properties of interstellar dust through the iron L-edges

BACHELOR THESIS

Author:
Scott Visser
6406165

Supervisors:
Prof. Dr. F.M.F de Groot
Debye Institute for Nanomaterials Science

Dr. L. Fillion
Debye Institute for Nanomaterials Science

Dr. E. Costantini
SRON, Netherlands Institute for Space Research



June 15, 2022

Cover image: The Lagoon Nebula is a place of spectacular star formation. Near the center of the image, one can see two long funnel-shaped dust clouds of roughly half a light-year long. These have been formed by intense stellar winds and energetic starlight. A remarkably bright star, Herschel 36, lights the area. Vast clouds of dust hide and redden other young stars everywhere in the image. The energetic starlight of these young stars forms temperature gradients in the cool dust and gas which can lead to shearing winds causing the funnels. This picture spans about 10 light-years and combines images taken in six colors by the Hubble space telescope. The Lagoon Nebula lies about 5000 light-years away from Earth toward the constellation of the Archer(Sagittarius).

(Image credit: M.H. Özşaraç; NASA, ESA, Hubble)

Abstract

The space in between the stars is filled with interstellar dust of which the physical and chemical properties are still not well understood. X-rays provide a powerful tool to probe the composition of this interstellar dust by measuring the radiation that it transmits. In order to understand the spectral signatures of interstellar dust we need to obtain reliable models using laboratory data. In this thesis we obtained transmission data for the iron L-edges for a set of interstellar dust analogues using EELS. Our analysis resulted in extinction, scattering and absorption cross sections for all dust analogues based on the MRN grain size distribution. We also looked at the effect of incorporating larger dust grains on the extinction cross sections and found that the cross sections show no new spectral features and that they have a stronger scattering component. Lastly, we show a simulated astrophysical spectrum of the future Athena mission, which will have superior capabilities with respect to present instruments. We can conclude that we found extinction models for interstellar dust around the iron L-edges with a resolution and signal-to-noise ratio that are sufficient to compare present and future astronomical data. These can help to fit future astronomical data and deepen our understanding of the properties of interstellar dust.

Contents

Layman's summary	1
1 Introduction	2
2 Theory and Methods	4
2.1 Electron Energy Loss Spectroscopy(EELS)	4
2.1.1 Interaction of highly energetic electrons with atoms	4
2.1.2 Structure of an EELS-spectrum	5
2.1.3 Extended Energy-Loss Fine Structure(EXELFS)	6
2.1.4 Iron L-edges	7
2.2 Laboratory experiment	8
2.2.1 Interstellar dust analogues	8
2.2.2 Analysing the laboratory data	9
2.3 From transmission data to atomic cross sections	11
2.3.1 Optical constants	11
2.3.2 Atomic scattering factors	12
2.3.3 Atomic cross sections	13
2.4 Implementation into dust models	14
2.4.1 Preparing the models for SPEX	14
2.4.2 Fitting astronomical data	15
3 Results & Discussion	16
3.1 From laboratory data to atomic cross sections	16
3.1.1 Optical constants	17
3.1.2 Atomic cross sections	19
3.2 Large grain size distribution	20
3.2.1 Absorption and scattering	21
3.2.2 Grain size distributions	22
3.3 Application to astronomical data	23
4 Conclusions & Outlook	26
Acknowledgements	27
References	28
A Extinction, scattering and absorption cross sections	I
B Extinction for both grain size distributions	II
C The ratio of absorption and scattering	III
D Normalization constants	IV

Layman's summary

Our Milky Way Galaxy is filled with billions of stars and the distance between these stars is enormous. The space in between the stars is filled with clouds made up of gas and dust, and this is referred to as the interstellar medium. This interstellar dust plays a key role in the way we see the light of other stars and how stars are formed. Moreover, these clouds are composed of the same materials as those that formed our solar system and the planet Earth so they could tell us more about our origin. Therefore, we would like to study the chemical composition of these clouds.

One studies this interstellar dust by measuring how much of the incoming light is transmitted when light hits such a dust cloud. Especially X-rays have very specific interactions with each chemical element which makes them a powerful probe. Using X-rays one can look at the presence of a single element in the dust. Here we focus specifically on certain features of the element iron. In this way, we can determine what kind and how much of an iron containing mineral is present in the interstellar medium. However, we do not know what the extinction of a certain mineral is, so it is important to develop a model to compare the astronomical data to.

Such a model can be obtained by measuring the transmission of a mineral in a laboratory on Earth. For the features that we were interested in we could use an electron microscope to measure the transmission. We chose a set of 14 types of dust samples that are expected to be present in the interstellar medium and did 5-10 measurements for each sample. Multiple measurements were done such that we could take an average and decrease the amount of noise in the data. After carefully calibrating the electron microscope and the resulting data we obtained a transmission spectrum for each measurement. The measured transmission could be used to calculate atomic cross sections. These are a measure of how strongly the sample absorbs and scatters light of a certain energy. The atomic cross sections could then be used to fit the astronomical data and give us a quantitative measure of the interstellar dust.

In order to obtain the atomic cross sections one has to assume some grain size distribution, called the MRN distribution, that specifies the number of grains with a certain size. However, this dust size distribution may not be representative for all environments in the Milky Way. Therefore, we also included a size distribution with larger dust grains. This would mimic more dense environments, for example close to the Galactic center.

Lastly, we used the calculated atomic cross sections to fit some simulated data from a future ESA(European Space Agency) mission, *Athena*. We used the specifications of this telescope to create an expected data set and fitted this with our calculated atomic cross sections.

1 Introduction

Nowadays, it is known that the space in between the stars in our Milky Way galaxy is not empty. There are all kinds of clouds containing gas and dust formed by a small set of elements and this is referred to as the interstellar medium (ISM). The dust grains in these clouds play a key role in the astrophysics of the ISM where they participate in star formation and absorb, scatter and reradiate electromagnetic radiation. Despite its importance there are some open questions concerning interstellar dust that remain.

In fact, much is unknown about the mineralogical composition of these dust clouds. For example, we do not know which types of silicates, olivines or pyroxenes, are most abundant in the ISM and how elements like Fe, S, O and C are incorporated in these grains [Mathis (1996)]. Furthermore, the presence of iron bearing silicates cannot explain the amount of iron locked up in dust grains. There are some theories to solve these problems such as GEMS (glass with embedded metal and sulfides) [Bradley (1994)] but these still need to be confirmed. In order to understand the astrophysics of the ISM and the spectral shapes of stellar bodies, it is crucial to improve our understanding of astronomical dust [Draine (2003)].

A powerful way to study the properties of interstellar dust grains is through high resolution X-ray spectroscopy. This became possible with the appearance of new and more modern telescopes, like the XMM-Newton¹ and Chandra² in the last century. Until recently, the physical and chemical properties of interstellar dust along different lines of sight in the Galaxy could only be studied using wavelengths ranging from radio to the ultraviolet [Whittet (2002)]. X-rays have some advantages compared to observing at the wavelengths from radio to the ultraviolet [Costantini and de Vries (2013)]. A wider range of column densities can be studied and we can probe different ionization states of elements. On top of that, we can investigate the shape, composition, crystallinity and grain size distribution of the interstellar dust in the ISM.

Each chemical element has a characteristic set of absorption edges and the X-ray absorption fine structure (XAFS) can be used to determine the mineralogy, size and shape of the grains [Corrales et al. (2019)]. Lab measurements of mineralogical candidates for astronomical dust are needed to be able to explain the astronomical data [Draine (2003)]. For this, Costantini and de Vries (2013) at SRON Leiden set up a large laboratory measurement campaign to measure the absorption edges of O, Si, Fe and Mg. They focus specifically on these elements because they are very abundant in the ISM and their absorption edges fall in the X-ray band of the currently available telescopes (0.2-10 keV).

Laboratory data for absorption edges in the soft X-rays energy regime (<1 keV) can be obtained with Electron Energy Loss Spectroscopy (EELS). With EELS one measures the inelastic scattering of electrons. At high kinetic energy and low scattering angle the spectral shape can be approximated with the dipole approximation which is identical to X-ray absorption [Egerton (2011), Miedema and de Groot (2013)]. The measured spectra can be converted into optical constants which are used to obtain absorption, scattering and extinction cross sections [Zeegers et al. (2017)]. These are the X-ray extinction models that can be implemented in a program called SPEX [Kaastra et al. (1996)] to analyse the astronomical data. Most of the edges of the mentioned elements have already been studied and only the iron L-edges remain (for the other edges see e.g. Zeegers et al. (2017), Rogantini et al. (2018), Psaradaki et al. (2020)). Therefore, we focus specifically on these iron L-edges.

¹<https://www.cosmos.esa.int/web/xmm-newton>

²<https://chandra.harvard.edu/>

The aim of this thesis is to obtain reliable X-ray extinction models for a set of 14 interstellar dust analogues in the energy range of the iron L2- and L3-edge at 720 eV and 707 eV, respectively. Moreover, we incorporate larger dust grains in the grain size distribution to see what the effect is on the extinction models and to model more dense galactic environments. Both types of models can then be used to investigate present and future astronomical data, and look at the iron content of interstellar dust.

In Section 2 we describe the theory behind EELS and the iron L-edges and how this can be used to determine an X-ray absorption model. We also show what kind of dust samples have been used and how the raw EELS data is processed. Then, in Section 3 we first check whether our code works as expected and obtain atomic scattering factors for all dust types. These are applied to both the MRN grain size distribution and an extended MRN size distribution. The models that were obtained are used to look at simulated astronomical data of the future *Athena*³ mission. Lastly, we give the conclusions of this research and a brief outlook in this field of research in Section 4.

³<https://sci.esa.int/web/athena>

2 Theory and Methods

In this section we describe the theory and methods needed to develop a model for the extinction cross section in the X-ray energy regime around the iron L-edges for different interstellar dust analogues. These models can be used to analyse astronomical data. First, we give an explanation of the theory behind EELS and the spectral signature of the iron L-edges. In Section 2.2 a description of the different dust types is given together with the processing of the laboratory data. Section 2.3 will present how to convert the laboratory transmission data into an extinction cross section for each dust sample. We conclude with a description of future astronomical data and how the extinction models need to be prepared to fit this data.

2.1 Electron Energy Loss Spectroscopy(EELS)

In EELS one uses a monoenergetic electron beam that interacts with a sufficiently thin sample (a few μm). This produces an energy distribution of the initially monoenergetic electrons. The electron microscope is often operated in STEM(Scanning Transmission Electron Microscopy) mode which means that one measures the electrons that are transmitted by the sample. This requires highly energetic(hundreds of keV) electrons that arrive perpendicular to the specimen such that virtually all electrons are transmitted.

These transmitted electrons interact with the atoms in the sample either elastically or inelastically. The inelastic scattering allows one to measure the energy loss of the electrons which results in a unique spectrum for each sample. In this work the theoretical framework of EELS was based on the book by [Egerton \(2011\)](#).

2.1.1 Interaction of highly energetic electrons with atoms

Before one dives into the application of EELS it is important to understand how it works. For this, the interaction of highly energetic electrons with atoms is crucial. As the incident electron beam is aimed at the sample the electrons scatter off the atoms in the sample. There are two types of scattering: elastic and inelastic scattering. Elastic scattering involves Coulomb attraction between the atomic nuclei and the incident electron. Inelastic scattering involves Coulomb repulsion between the atomic electrons and the incident electron beam(Fig. 1).

In elastic scattering(Fig. 1(a)) the electron does not lose any energy and this is also known as Rutherford scattering. This type of scattering usually has a much higher probability to occur than the inelastic scattering so the resulting *zero-loss* peak(ZLP) is much stronger than the inelastic features of the spectrum. Therefore, the ZLP is filtered out to be able to focus more on the much weaker inelastic part. Nevertheless, because the initial energy of the electron beam is known the ZLP can be used as an internal calibration for the energy axis of different measurements.

For inelastic scattering the incident electron interacts either with an *inner-shell* electron (Fig. 1(b)) or with an *outer-shell* electron(Fig. 1(c)). In the first case, the *inner-shell* electron is excited to an empty atomic orbital for which some hundreds to thousands of electron volts are needed. The incident electron provides this energy which is relatively small compared to the energy of the electron beam which is hundreds of keV. After the scattering event, the atom is in an excited state and relaxes through a downward transition of an *outer-shell* electron to the vacant “core-hole”. The energy that is released during this de-excitation is emitted as electromagnetic radiation(X-rays) or as kinetic energy of another atomic electron(Auger electron).

The inelastic scattering with *outer-shell* electrons follows the same principles but it involves a smaller energy transfer. The de-excitation mainly creates heat and sometimes electromagnetic radiation in the visible region. An alternative is *outer-shell* inelastic scattering where many atoms are involved instead of one. This causes a collective oscillation of atomic electrons and is known as plasma resonance. In general, this is described as a pseudoparticle, a plasmon, which is a travelling wave in the solid.

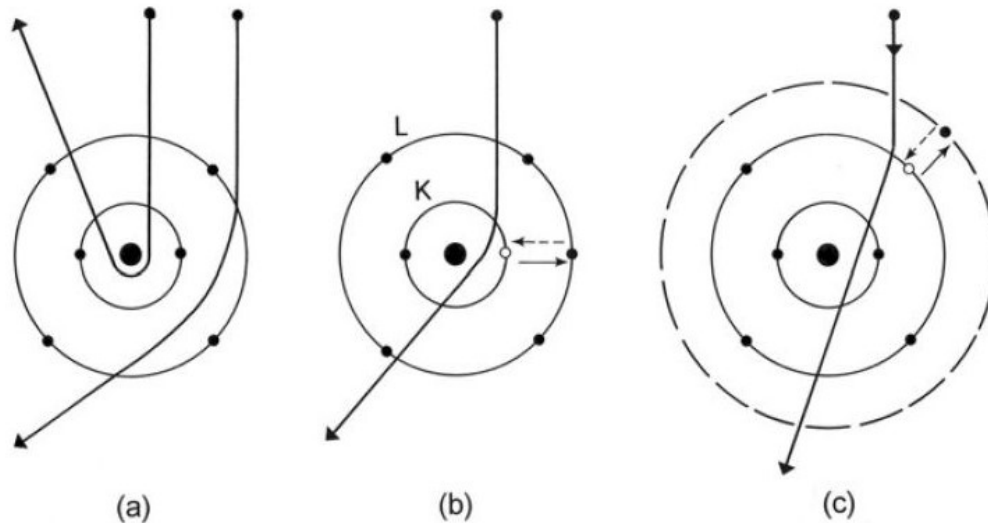


Figure 1: A classical view of electron scattering by a single atom. (a) Elastic scattering is caused by Coulomb attraction between the nucleus and the incident electron. Inelastic scattering results from Coulomb repulsion between the incident electron and (b) inner- or (c) outer-shell electrons. These atomic electrons are excited to a higher energy state. The reverse transitions are shown by broken arrows[Egerton (2011)].

2.1.2 Structure of an EELS-spectrum

All of the possible interactions mentioned above result in a typical shape of an EELS-spectrum. In general, an EELS-spectrum contains a very strong ZLP at 0 eV, a number of *low-loss* features and the much weaker absorption edges. An EELS-spectrum for iron oxide nanoparticles can be seen in Fig. 2 which indicates all of these features. The ZLP is clearly much larger than the other features due to the higher scattering probability. The high kinetic energy of the electrons causes the excitation of all kinds of inelastic processes that form the *low-loss* region(0-50 eV). These features can be caused by the creation of phonons(0-0.2 eV), dd-excitations(0-5 eV), charge transfer excitations and plasmon resonances(4-40 eV). Due to all of these different processes and corresponding energy losses there is a broad band visible in the *low-loss* region.

The interesting inelastic features are the absorption edges of the elements that are present. These are the features that depend on the type of specimen and the types of elements they contain. Edges are named after the element they belong to and the atomic shell(K,L,M, etc.) that the atomic electron was in before the inelastic scattering event occurred. The probability of inelastic scattering is much smaller so one needs long exposure times in order to be able to collect enough electron counts.

The absorption edges represent the probability for inelastic scattering with a certain element to occur and this gives rise to a typical *saw-tooth* shape on top of a sloping curve. The probability

has a slope because a higher energy loss is just less probable. This continues until the right energy, the *ionization threshold*, for a certain element is reached and the probability peaks. After that, the probability drops but it stays higher than in the pre-edge region because the electrons with higher energies can still excite the core electrons. After the edge, the sloping curve takes over again. The width of these edges is governed by the time-energy uncertainty relation,

$$\Delta E \Delta t \geq \frac{\hbar}{2} \quad (1)$$

with ΔE the energy spread, Δt the temporal uncertainty and $\hbar \equiv h/2\pi$ where h is Planck's constant. Quantum mechanics tells us that the finite lifetime of the excited state leads to an energy uncertainty of a few hundreds of meV. For the iron L-edges the broadening is typically 0.4 eV where for the L2-edge there is some extra broadening due to the super-Coster-Kronig Auger decay[Coster and de L. Kronig (1935), de Groot et al. (2021)].

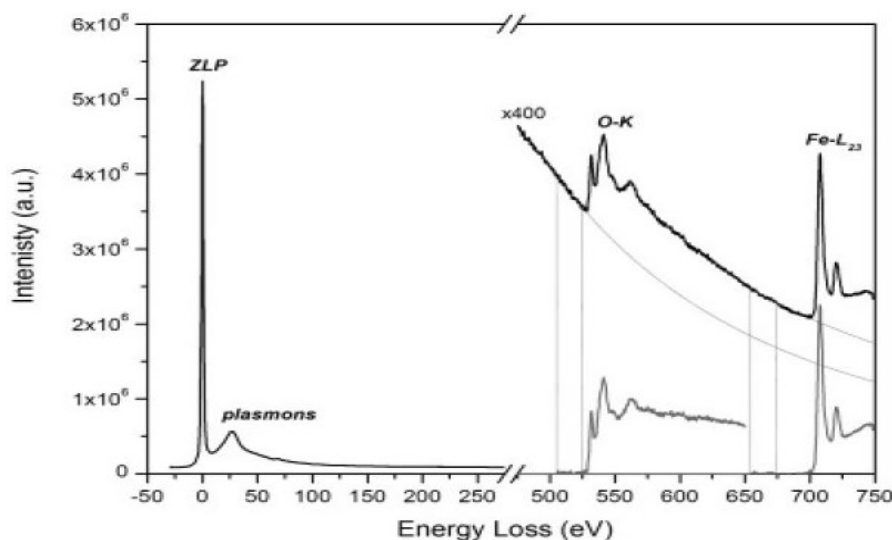


Figure 2: An EELS-spectrum measured for a large iron oxide nanoparticle($\sim 10 - 40$ nm). The zero-loss peak(ZLP) and the band in the low-loss region are clearly visible. The oxygen K-edge and iron L-edges are enhanced in order to see them better[Jasinski et al. (2006)].

2.1.3 Extended Energy-Loss Fine Structure(EXELFS)

The wave character of the ejected core electrons allows for interference with the surrounding atoms such that the chemical environment of the atom can be probed. When the ejected core electron has a kinetic energy of more than 50 eV it behaves much like a free electron. According to quantum mechanics, this can be seen as a spherical wave emanating from the atom. If the atom is isolated then we see a clean edge without any fine structure because there is no interference, see panel (a) of Fig. 3.

However, weak oscillations can arise from interference between the outgoing spherical wave and the reflected waves due to elastic backscattering from neighboring atoms. These oscillations in intensity can be seen in panel (b) of Fig. 3 and can extend across several hundred electron volts after the ionization edge. The EXELFS pattern depends on the type of element and on the position of neighboring atoms. In theory, this could help to identify the chemical structure of the compound that you are studying and can be used to identify interstellar dust[Egerton (2011)].

2 THEORY AND METHODS

Note that one uses the term X-ray absorption fine structure(XAFS) when the absorption of X-rays is studied.

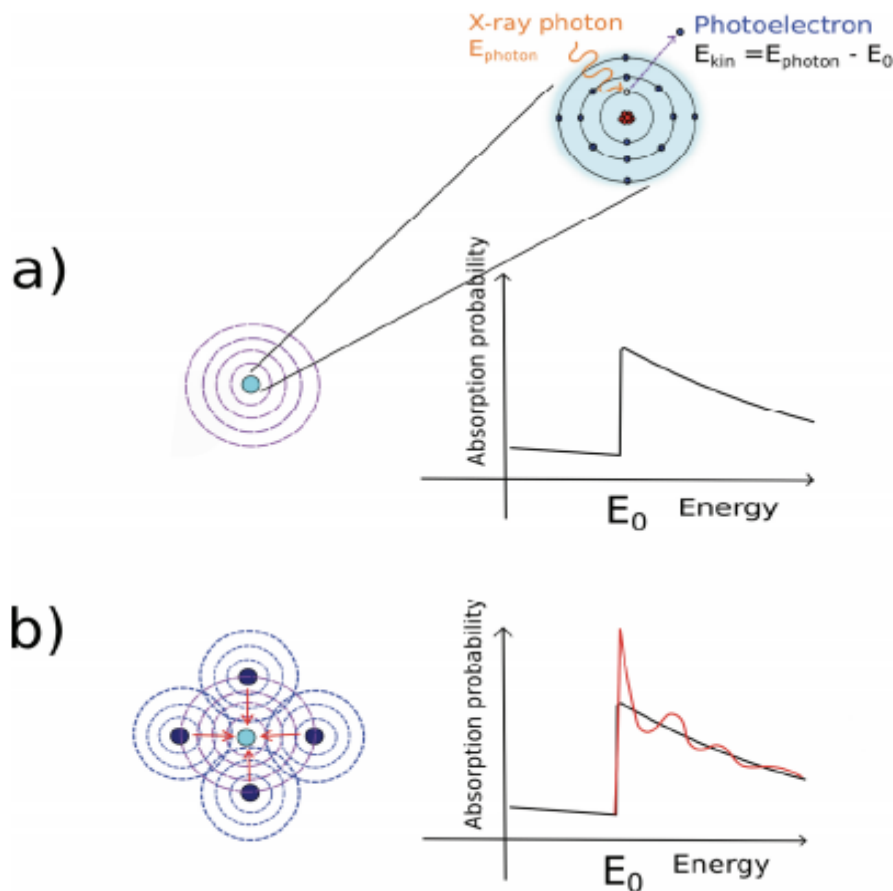


Figure 3: Illustration of: a) A photoabsorption edge of an isolated atom. b) The XAFS in the case of multiple atoms where the absorption probability is modified because of interference with the spherical wave. (Credit: S. Zeegers)

2.1.4 Iron L-edges

In this work we focus specifically on the iron L-edges. In the *energy-loss* spectrum, these edges can be found at 706.8 eV, 719.9 eV and 844.6 eV for the L3-, L2- and L1-edge, respectively[Fuggle and Mårtensson (1980)]. The iron L-edges also have a fixed absorption cross section ratio, or *branching ratio*, which is L3:L2:L1 = 1:0.48:0.17 for pure iron in gaseous form[Verner et al. (1996)]. Note that the *branching ratio* depends on the valency and spin-state of the iron atom and is different for every system[Colliex et al. (1991)]. The exact energies of the edges can differ somewhat between different samples but these chemical shifts are of the order of a few hundred meV and not so important for our study. One can find the L2- and L3-edge of iron in Fig. 2.

The ground state of the iron atom has quantum numbers $L = 2$ for angular momentum and $S = 2$ for the spin. The iron L-edges are produced when either a $2s^2$ core electron or a $2p^6$ core electron is excited. Within the dipole approximation the electrons are only allowed to go to certain orbitals according to the dipole selection rule $\Delta J = 0, \pm 1$ where $J = L + S$. This means that $2s$ -electrons can only go to a p -orbital and the $2p$ -electrons can only go to a s - or d -orbital[Miedema and de Groot (2013)].

2 THEORY AND METHODS

In Section 2.2.1, one sees that the dust samples fall mainly in the group of iron containing silicates. Therefore, we have Fe^{2+} ions with an electron configuration of $[\text{Ar}]3d^6$. The L1-edge is formed when a transition from a $2s^2$ core state occurs and the L2- and L3-edge are formed by a $2p^63d^6 \rightarrow 2p^53d^7$ transition. The $2s^2$ electrons in iron are more strongly bound to the nucleus than the $2p^6$ electrons so this explains why the L1-edge is found at a higher energy than the L2- and L3-edge. Due to $2p$ spin-orbit coupling the $2p^63d^6 \rightarrow 2p^53d^7$ transition splits into two because of the $2p_{3/2}$ and $2p_{1/2}$ states of the $2p$ -orbital. This spin-orbit coupling is quite large and splits the spectrum into the L2- and L3-components with a relative separation of 13.1 eV.

The $3d$ spin-orbit coupling then leads to a splitting into states with the quantum number J equal to 4, 3, 2, 1 and 0 from low to high energy. This splitting results in different energy levels separated by tens of meV. In order to find the resulting theoretical spectrum one should use a Boltzmann distribution and combine all five states. In reality, an experiment will always result in a combination of all components weighted by the Boltzmann distribution such that it is impossible to resolve the separate states[Miedema and de Groot (2013)]. In theory, one can use this to determine the $3d$ spin-orbit splitting since the spectral shape will reveal this. We do not expect to be able to do this because of the resolution in our experiment(see Section 2.2.1).

2.2 Laboratory experiment

In order to determine what kind of chemical compounds are present in interstellar dust one needs dust models to compare the astronomical data to. For this reason, a large laboratory measurement campaign was set up to characterize the X-ray absorption edges of many interstellar dust analogues[Costantini and de Vries (2013)]. In this thesis we present a set of 14 interstellar dust analogues that contain iron, see Table 1. We measure the EELS spectrum of each compound in the energy regime around the iron L-edges and prepare this data for our calculations.

2.2.1 Interstellar dust analogues

Studies of the astronomical IR(infrared) band showed that the stoichiometry of silicate dust is mostly amorphous olivines($\text{Mg}_{2-x}\text{Fe}_x\text{SiO}_4$) and amorphous pyroxenes($\text{Mg}_{1-x}\text{Fe}_x\text{SiO}_3$) where $0 \leq x \leq 1$ [Min et al. (2007)]. For this reason, the set of compounds presented here contains both amorphous and crystalline samples and fall mostly in the groups of silicates. Moreover, we also include some other types of materials like magnetite, metallic iron and samples containing sulphur to get a more complete set of models.

Here amorphous means that the sample is *non-crystalline* such that it lacks any long-range order. The dust in the ISM is expected to be mostly amorphous because crystalline dust is unlikely to survive for very long in the harsh conditions of the ISM[Jones and Nuth (2011)].

Pyroxenes and olivines with different Mg:Fe ratios are chosen to see which one can fit the astronomical data best. Olivines can vary between Mg_2SiO_4 (forsterite) and Fe_2SiO_4 (fayalite). Pyroxenes range from Mg-pure MgSiO_3 (enstatite) up to Fe-pure FeSiO_3 (ferrosilite). For this reason, pyroxene samples are named according to $\text{En}(z)\text{Fs}(1-z)$ where 'En' stands for enstatite, 'Fs' stands for ferrosilite and z is the percentage of Mg present[Rogantini et al. (2019)].

The dust samples in Table 1 are laboratory analogues and have different origins. Sample 2 is a commercial product, samples 3 and 6 are natural minerals and sample 13 is of meteoritic origin. The other samples, except metallic iron, were all synthesized in the laboratories at the Astrophysikalisches Institut, Universitäts-Stenwarte(AIU) and Osaka University(for details see

Zeegers et al. (2019)). The data for metallic iron is literature data and comes from the article by Kortright and Kim (2000).

Sample number	Compound name	Stoichiometry	Molecular mass (g/mol)	Density (g/cm ³)	Form
1	Fayalite	Fe ₂ SiO ₄	203.77	4.39	Crystalline
2	Magnetite	Fe ₃ O ₄	231.51	5.17	Crystalline
3	Hyperstene	Mg _{1.502} Fe _{0.498} Si ₂ O ₆	216.50	3.34	Amorphous
4	En75Fs25	Mg _{0.75} Fe _{0.25} SiO ₃	108.28	3.34	Crystalline
5	Olivine	MgFeSiO ₄	149.83	3.12	Amorphous
6	Olivine	Mg _{1.56} Fe _{0.4} Si _{0.91} O ₄	172.23	3.12	Crystalline
7	En90Fs10	Mg _{0.9} Fe _{0.1} SiO ₃	103.55	3.25	Amorphous
8	En90Fs10	Mg _{0.9} Fe _{0.1} SiO ₃	103.55	3.25	Crystalline
9	En60Fs40	Mg _{0.6} Fe _{0.4} SiO ₃	113.01	3.42	Amorphous
10	En60Fs40	Mg _{0.6} Fe _{0.4} SiO ₃	113.01	3.42	Crystalline
11	Pyrrhotite	Fe _{0.87} S	647.43	4.60	Crystalline
12	Pyrite	FeS ₂	119.98	5.01	Crystalline
13	Troilite	FeS	87.91	4.65	Crystalline
14	Metallic iron	Fe	55.85	7.60	Crystalline

Table 1: A list of the interstellar dust analogues that are used.

For obtaining EELS spectra of the dust analogues, the STEM facility at the University of Cadiz is used. In this experiment we use the Titan Cubed Themis 60-300 microscope in STEM mode, operating at 200 keV. In parallel, high-spatial resolution EELS spectra are recorded with the spectrum-imaging mode which allows for the correlation of analytical and structural information on different regions of the dust sample. With this we can compare the spectra with the spatial distribution of the sample. The experiments are done in Dual EELS mode using an energy dispersion of 0.25 eV, 50 pA probe current and 50 ms acquisition time per EELS spectrum. The STEM mode of the electron microscope enables us to scan the dust samples pixel by pixel. The resulting spectrum will be the average of each pixel on the CCD(charge-coupled device) detector. To improve the signal-to-noise ratio(SNR) of the data, we obtain 5-10 measurements of each specimen, focusing on different regions of interest[Manzorro et al. (2019),Psaradaki et al. (2020)].

2.2.2 Analysing the laboratory data

The electron counts data that is collected in STEM mode first needs to be processed in order to be useful as transmission data. The steps that are needed in the analysis are essentially the same as was presented by Psaradaki et al. (2020). The difference is that in their article Psaradaki et al. (2020) focused on the oxygen K-edge around 550 eV and we focus on the iron L-edges around 710 eV. The laboratory data is converted to a python-readable format using the *hyperspy* package⁴. Then the analysis consists of five steps:

⁴<http://hyperspy.org/hyperspy-doc/current/index.html>

1. *Thickness selection*: The dust samples have an intrinsic size variation so in order to be consistent and to be optically thin a thickness selection needs to be done. For this, the thickness of the sample in each pixel was determined using

$$t = \log_{10} \left(\frac{I_{\text{core-loss}}}{I_{\text{zero-loss}}} \right) \quad (2)$$

for that specific pixel. Here $I_{\text{core-loss}}$ is the intensity of the *core-loss* peak (inelastic scattering) and $I_{\text{zero-loss}}$ is the intensity of the *zero-loss* peak (elastic scattering). Note that this is a sort of optical thickness as seen by the electron microscope and not an absolute physical thickness. In EELS the interaction of the sample with the incident electrons becomes stronger as the thickness increases. This will result in multiple-scattering events which reduce the SNR [Parratt et al. (1957), Bunker (2010)]. Therefore, the part of the grain where $t/\tilde{\lambda} > 0.3$ is excluded. Here $\tilde{\lambda}$ is the mean free path of the inelastic scattering in μm which depends on the material.

2. *Spectrum alignment*: In an EELS experiment it is important to align the energy axis of the spectrum for different measurements. To achieve this, one obtains the *low-loss* spectrum that contains the ZLP. The position of the ZLP does not depend on the sample and can thus be used to align the different spectra. Note that this is a relative energy calibration between separate measurements and not an absolute one.
3. *Background subtraction*: The sloping effect of the EELS background is removed by fitting a second order polynomial to the data and subtracting this. The polynomial is fitted to the part of the spectrum in between the oxygen K-edge and the iron L-edges, approximately from 570 eV up to 700 eV.
4. *Energy calibration*: In EELS experiments one needs to carefully consider the absolute energy calibration of the measured spectrum. The calibration of the detector could be imperfect so for absolute values an internal verification is needed. In the recorded spectra a pre-peak of the oxygen K-edge seems to be present. It is believed that this feature corresponds to an electronic transition in molecular oxygen (O_2). Oxygen is thought to evaporate because of the impact of the incident electron beam on the sample. A value of 530.5 eV is adopted as an absolute energy and all energy axes are shifted to align with the energy of this feature [Jiang and Spence (2006), Garvie (2010)]. This yields two points to calibrate the energy axis with, the ZLP at 0 eV and the oxygen pre-peak at 530.5 eV.
5. *Principal Component Analysis (PCA)*: When the SNR allows it, a PCA can be used to test whether the samples were homogeneous in composition and thickness. A PCA is a statistical procedure that decomposes a data set into an orthonormal basis of principal components. These principal components are lines that fit the data best based on minimizing the average squared distance to the data points. The spectral components describe the variability of the data where the first component explains the most variance, the second component explains the most variance of what is left and so on. Each component is orthogonal to the others and there are exactly as many components as there are variables. This will reveal characteristic features of the spectrum in order of variation and is useful for reducing the dimensionality of the data set. In this way, one can obtain robust results and avoid artefacts in the data [Pearson (1901), Psaradaki et al. (2020)]. However, since we do such a severe thickness selection the amount of data that is left could be too small to do a PCA. Only data sets with a good SNR will be able to generate a PCA and it is difficult to predict when this is the case.

2 THEORY AND METHODS

2.3 From transmission data to atomic cross sections

In order to be able to implement the laboratory data into the fitting program for interstellar dust we need to obtain atomic cross sections of all dust types. Again, in the dipole approximation the data obtained by EELS will be the same as the X-ray absorption spectrum of a material. Therefore, we can use the EELS spectra as transmission data to obtain atomic cross sections. First, we need to determine the optical constants of each dust type which can be converted to atomic scattering factors. These can be used to calculate atomic cross sections based on different grain size distributions. This procedure has been described extensively in the articles by Zeegers et al. (2017), Rogantini et al. (2018) and Psaradaki et al. (2020).

2.3.1 Optical constants

In this research, the focus lies on the absorption of X-rays which are electromagnetic radiation. When these travel through a material they can either be transmitted, absorbed or scattered. The transmittance of light by a solid is given by the Lambert-Beer law,

$$T = \frac{I}{I_0} = e^{x\mu(E)} = e^{x/\tilde{\lambda}} \quad (3)$$

with T the transmittance, I the transmitted intensity, I_0 the incident intensity, x the thickness of the sample in μm and μ the attenuation coefficient in μm^{-1} as a function of energy E . By applying the Lambert-Beer law we ignore reflection of the X-rays at the grain surface, which is a good approximation for X-rays. Only then is the attenuation coefficient the same as the absorption coefficient. Using this, the attenuation coefficient is approximately given by the sum of the different elemental cross sections in the material such that

$$\mu(E) \approx \sum_i \rho_i \sigma_i = \rho_M \sum_i \frac{m_i}{M} \sigma_i \quad (4)$$

where ρ_M is the mass density of the compound, m_i/M is the fractional mass contribution of element i and σ_i is the mass normalised absorption cross section. For our samples it is important that the selected thickness is below 2-3 absorption lengths ($\tilde{\lambda}$) to minimize thickness effects. This is guaranteed by the thickness selection as explained in Section 2.2.2.

To calculate the absolute extinction cross section, the refractive index needs to be determined. The complex refractive index m is given by $m = n + ik$ where n and k are the real and imaginary part, also referred to as optical constants. The imaginary part of the refractive index depends on the attenuation coefficient through

$$k = \frac{\mu\lambda}{4\pi} \text{ with } \mu(E) = \frac{-\ln(T)}{x} \quad (5)$$

where λ is the wavelength in μm calculated by

$$\lambda = \frac{hc}{E} \quad (6)$$

with c the speed of light. Initially, the absolute thickness of the sample in each measurement is not known. Therefore, the data is normalized using the tabulated values provided by the Center for X-ray Optics at Lawrence Berkeley National Laboratory (CXRO)⁵ which are described in Henke et al. (1993). These tabulated values of the transmission are calculated at certain energies over a range of 10 to 30.000 eV for a well defined physical thickness.

⁵<http://www.cxro.lbl.gov/>

2.3.2 Atomic scattering factors

Another, commonly used formulation are the atomic scattering factors f_1 and f_2 [Henke et al. (1993)]

$$f(E) = f_1 + if_2 = \frac{2\pi A}{\rho N_A r_0} \frac{1}{\lambda^2} (m - 1) \quad (7)$$

which are related to the optical constants by [Rogantini et al. (2018)]

$$\begin{aligned} n(E) &= 1 - \frac{\rho N_A r_0}{2\pi A} \lambda^2 f_1(E) \\ k(E) &= \frac{\rho N_A r_0}{2\pi A} \lambda^2 f_2(E) \end{aligned} \quad (8)$$

where N_A is Avogadro's number, A is the atomic mass number of the compound, ρ is the density in g/cm³ and r_0 is the classical electron radius.

As can be seen in Eq. 8, one can calculate the imaginary part of the atomic scattering factor directly by using k . However, this cannot be done for the real part (f_1) since n is not known. Luckily, the real and imaginary part of the atomic scattering factor are not independent. To determine the real part of the refractive index one can make use of a numerical solution to the Kramers-Kronig relations in Eq. 9 [Bohren (2010)]. These relations connect the real part of a complex function to its imaginary part. This is only possible for a complex function of ω that is analytic in the closed upper half-plane of ω and vanishes faster than $1/|\omega|$. An analytic function in a region R of the complex plane is defined as a function that is single valued and has a derivative at each point in R . If this is true, one can calculate the real part of the atomic scattering factor using the imaginary part. This is done by evaluating the following integral from Thompson et al. (2001)

$$f_1(E) = Z^* - \frac{2}{\pi} P \int_0^\infty \frac{\omega f_2(\omega)}{\omega^2 - E^2} d\omega \quad (9)$$

where ω is the integration variable, E is the energy at which the real part of the atomic scattering factor is evaluated, Z^* is the relativistic correction and P indicates that the Cauchy principal value is to be taken [Landau and Lifshitz (1960)]. In our case ω represents all energies.

An important part in Eq. 9 is the relativistic correction. When we take relativistic effects into account, Z^* is slightly lower than Z , the atomic number. The difference is approximately equal to E_{tot}/mc^2 with E_{tot} the atomic binding energy. In order to be accurate, we cannot simply use Z and a correction is needed which is mainly significant for the high Z elements. Henke et al. (1993) have fitted values of the difference, $Z - Z^*$, to find that the relativistic correction is fitted best by

$$Z^* = \sum_q n_q \left[Z_q - \left(\frac{Z_q}{82.5} \right)^{2.37} \right] \quad (10)$$

where n_q and Z_q represent the number density and the atomic number of the q^{th} element in the material, respectively.

There are two problems with the integral in Eq. 9. First, it spans from 0 to infinity and $f_2(\omega)$ is not known over this entire range. Secondly, the integral contains a discontinuity at $\omega = E$ and must therefore be considered as a Cauchy principal value. The Cauchy principal value is a mathematical method for assigning values to certain improper integrals which would otherwise

be undefined. The result of this is that we have to include the factor of P . There are several solutions to these problems but here the extension of the [Henke et al. \(1993\)](#) approach by [Watts \(2014\)](#) was used. This method has been implemented in a python library called *kkcalc*⁶. This algorithm is computationally fast and its accuracy is limited only by the representation of the absorption spectrum by a piecewise set of Laurent polynomials.

2.3.3 Atomic cross sections

Finally, we have to calculate the extinction cross section for each sample using the atomic scattering factors. Note that these are not physical cross sections but optical cross sections to quantify the degree of interaction with the incident radiation. There are different methods to compute the extinction cross section like Rayleigh-Gans, Mie theory [[Mie \(1908\)](#)] and Anomalous Diffraction Theory (ADT) by [van de Hulst \(1958\)](#). It depends on the particle size and energy range which method works best [[Hoffman and Draine \(2016\)](#)].

To calculate the extinction cross sections we use the ADT formulation. ADT is a simplification of the complete Mie theory both in concept and in efficiency of computation. It is applicable to dust grains of any geometry that fulfill the requirements that $|m - 1| \ll 1$ and $x = 2\pi a/\lambda \gg 1$ where a is the effective radius of the grain. In other words, the dust grain needs to be optically soft and larger than the wavelength of the incident X-ray. Based on these assumptions, ADT calculates the efficiency factors for extinction and absorption per grain size for each energy. The scattering efficiency cannot be calculated directly but can be found using the other two efficiencies. To this end, the following equations expressed in terms of n , k and x are used

$$\begin{aligned} Q_{ext} &= 2 + 4 \left[\frac{\cos(2\beta) - e^{-2xk} \cos(2x(n-1) - 2\beta) + 2x\sqrt{\alpha} \sin(2x(n-1) - \beta)}{4x^2\alpha} \right] \\ Q_{abs} &= 1 + \frac{e^{-4xk}}{2xk} + \frac{1}{2} \frac{e^{-4xk} - 1}{(2xk)^2} \\ Q_{sca} &= Q_{ext} - Q_{abs} \end{aligned} \quad (11)$$

where $\alpha = (n-1)^2 + k^2$ and $\beta = \arccos[(n-1)/\sqrt{\alpha}]$.

To obtain the total cross section per wavelength unit, we need to integrate over the grain size distribution which gives

$$\sigma_j(E) = \int_{a_-}^{a_+} Q_j(a, E) n(a) da \quad (12)$$

where $n(a)$ is the grain size distribution as a function of grain radius, a_{\pm} are the maximum and minimum grain radius and j refers to absorption, scattering or extinction. A grain size distribution tells you how many particles there are of a certain size in the ISM. The mathematical form of the grain size distribution is not exactly known but different forms have been tried to find the best [[Mathis et al. \(1977\)](#)]. Through the years, different grain size distributions have been suggested but one often uses a grain size distribution that has the form of a power law as a function of a , i.e. $n(a) \propto a^{-q}$. There is not one distribution that fits the interstellar dust perfectly so a simple power law is often preferred because it is easy to implement in numerical programs and it is reasonably good.

⁶<https://pypi.org/project/kkcalc/>

Such a distribution is the Mathis-Rumpl-Nordsieck(MRN) distribution by Mathis et al. (1977) with a grain size interval of $0.005 \leq a \leq 0.25 \mu\text{m}$ and $q = -3.5$. This will give us a grain number density of the form [Mauche and Gorenstein (1986)]

$$n(a)da = A_i n_H a^q da = A_i n_H a^{-3.5} da \quad (13)$$

where n_H is the number density of H atoms and A_i is the normalization constant which depends on the type of dust in $\text{cm}^{2.5}$. Here A_i is calculated following the method by Mauche and Gorenstein (1986) such that

$$A_i = \log_{10} \left(\frac{5.83 \cdot 10^{-23}}{n_H \sigma_{i,\text{sca}}} \right) \quad (14)$$

where the constant $5.83 \cdot 10^{-23} \text{ cm}$ is a mean extinction per kiloparsec in space. This method makes use of the Rayleigh-Gans approximation, i.e. $4\pi a|m-1| \ll \lambda$, just as was done in ADT. The calculations give us cross sections in cm^2 per hydrogen nucleus present in the ISM.

Somehow, this grain size distribution does not always seem able to explain all of the features in the astronomical data. For some lines of sight there may be more dense environments in the Galaxy. For example, close to the Galactic center the density of dust clouds becomes larger such that the grains also become larger. It could be possible that a grain size interval of $0.005 \leq a \leq 0.25 \mu\text{m}$ is too narrow for some parts of the ISM. Therefore, a wider grain size distribution with a grain size interval of $0.05 \leq a \leq 0.50 \mu\text{m}$ was used.⁷ Note that this still is the MRN size distribution with the form of a power law but now the grain size window is larger. One would not expect the dust particles to be much larger than $0.50 \mu\text{m}$ since collisions with highly energetic radiation will keep the dust particles from becoming larger.

2.4 Implementation into dust models

For the final step, we need to prepare the extinction, absorption and scattering cross section of each dust type for their application in the program SPEX, version 3.06.01⁸ [Kaastra et al. (1996), Kaastra et al. (2020)]. SPEX is optimized to analyse and interpret high resolution cosmic X-ray spectra. It is especially suited for fitting spectra obtained by X-ray observatories like XMM-Newton, Chandra, Suzaku and Hitomi and will be improved to handle the spectra of future missions like Athena.⁹

2.4.1 Preparing the models for SPEX

The idea is that we paste the found extinction cross sections onto an overall background, represented by Verner cross sections [Verner et al. (1996)], in SPEX. These models can then be fitted to the astronomical data of the iron L-edges. The preparation of the cross sections starts with a renormalization. We need to renormalize them such that they are not measured per H nucleus but per Fe nucleus. For this we use the solar abundance of Fe which is $3.265 \cdot 10^{-5} H^{-1}$ from Lodders et al. (2009). Solar abundances are always measured with respect to the abundance of hydrogen and can be calculated using

$$\log_{10}(A_{\text{Fe}}) = \log_{10}(N_H) + \log_{10}(N_{\text{Fe}}/N_H) \quad (15)$$

⁷Hereafter, we refer to this as 'the large grain size distribution'.

⁸<https://zenodo.org/record/4384188>

⁹<https://www.sron.nl/astrophysics-spex>

where $N_H = 10^{12}$ is the so-called hydrogen column density and N_{Fe} the iron column density [Rogantini et al. (2019)].

The second step is to remove the underlying background of the Henke tables and any slopes from the data [Henke et al. (1993)]. The pre-edge and post-edge parts of the cross sections should be horizontal and we smooth out any noise artefacts such that we get smooth cross section curves. This puts the cross section of the pre-edge region at zero. Moreover, we need to convert the units from cm^2 to Mbarn where we use that $1 \text{ cm}^2 = 10^{18} \text{ Mbarn}$.

Finally, we have to project the cross section data on a regular SPEX grid, again make sure that we use the units applied in SPEX and force the data to connect smoothly at its end points to the overall background. After all of these steps we can implement the extinction cross sections into the interstellar dust absorption model (AMOL) of SPEX. Note that there is a slight difference between the models because SPEX uses the Verner cross sections and not the Henke cross sections. However, this is expected to fall within the limit of precision that can be achieved in observations so it will not affect the analysis.

2.4.2 Fitting astronomical data

Now that we have obtained extinction cross sections for the different dust types we can start to fit astronomical data around the iron L-edges. For this, we simulate data of the future *Athena* mission. This means that we simulate astronomical data with the spectral resolution and effective area of *Athena*. This can already give us an idea of the research that is possible with this mission and we can see whether our extinction models are good enough.

Athena (Advanced Telescope for High Energy Astrophysics) is a future X-ray telescope of the European Space Agency (ESA) which is expected to launch around the year 2031. *Athena* is supposed to help us better understand the hot and energetic Universe using its large effective area and a spectral resolution of 2.5 eV in the 0.2-12 keV energy band. These specifications are far better than those of currently used telescopes. With *Athena* the interstellar dust properties can be studied in detail in the hard X-ray band and it improves resolution in the soft X-rays [Nandra et al. (2013), Barret et al. (2016)].

With SPEX we can look at both simulated data of *Athena* and real astronomical data recorded by the currently used RGS spectrometer of XMM-*Newton*. In this way, we can compare both data sets and see where *Athena* can help us understand interstellar dust better.

When one looks at astronomical data it is important to be as realistic as possible. In our Galaxy, the X-rays of a certain background source have to travel a large distance before reaching our detector. Across this vast distance it will encounter multiple clouds of gas and dust with different temperatures and densities. The grain size distribution will explain dust component but there is also a lot of gas. This collisionally ionized gas absorbs X-rays as well and we have to take this into account when looking at both real and simulated data.

3 Results & Discussion

In this section we present the results of the different steps described in Section 2. In the text we focus specifically on the results of amorphous olivine(sample number 5) because of its astronomical importance and clear data. The data of the other samples can be found in the Appendix. First, in Section 3.1 we describe the analysis as described in Section 2.2.2 and 2.3 and verify whether our code works correctly. Next, in Section 3.2 we use the obtained data to see the effect of using a larger grain size interval than in the original MRN distribution. Lastly, in Section 3.3 we use the obtained dust models to analyse astronomical data from the *Athena* mission using SPEX.

3.1 From laboratory data to atomic cross sections

As explained in Section 2.2, 5-10 EELS measurements of different areas on each sample were done. This resulted in a data file for each measurement that contained data on the spatial dimensions(x,y), the electron energy loss, the *low-loss(zero-loss)* peak and the intensity for all pixels on the CCD detector. The thickness of the sample in each pixel was determined by using Eq. 2 for that specific pixel. Again, note that this thickness is not a physical thickness but more of an optical thickness as seen by the detector.

An example of the resulting thickness graph for amorphous olivine can be seen in Fig. 4 where one clearly sees the edge of the dust grain. Similarly, thickness profiles were obtained for all measurements of all samples. These were all quite different due to different grain geometries, locations on the sample and dust types. Note that this is the raw data so no thickness selection or any other data processing has been applied yet.

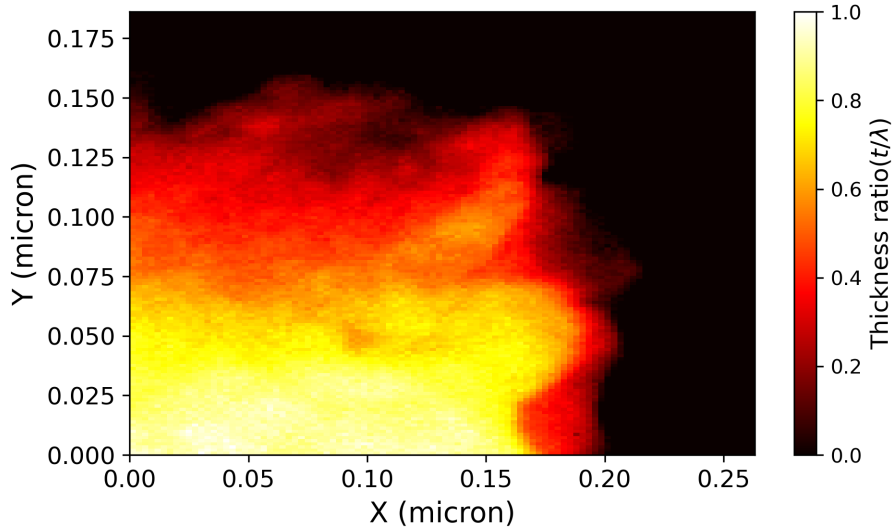


Figure 4: A thickness plot for a measurement of the amorphous olivine dust sample obtained from STEM laboratory data. The colorbar indicates the thickness ratio $t/\tilde{\lambda}$ where t is the thickness and $\tilde{\lambda}$ the mean free path of the inelastic scattering.

The obtained thickness profiles were processed as described in Section 2.2.2 which involved the thickness selection, spectrum alignment, background subtraction, energy calibration and PCA. After all of these steps the resulting data looked like that in Fig. 5. We see in Fig. 5a that requiring that $0 \leq t/\tilde{\lambda} \leq 0.3$ results in a lot of data loss which reduces the SNR heavily.

3 RESULTS & DISCUSSION

Therefore, it was not possible to do a PCA for most measurements. Since there were so few measurements that could generate a PCA it was difficult to interpret the ones that did allow for a PCA.

In Fig. 5b one sees a graph of the recorded intensity in an energy range around the oxygen K-edge(550 eV) and iron L-edges(707 and 720 eV). This spectrum shows clear edges and has a reasonably good SNR compared to other measurements. On the other hand, there were also measurements which had barely any signal left after the data processing. The really bad data sets had to be discarded to prevent the introduction of a lot of noise.

The procedure described in Section 2.2.2 like the thickness selection, background subtraction and energy calibration contained some steps that had to be done manually. This resulted in some uncertainties which are difficult to quantify. Most subtle differences that will arise are minimized when one averages over all the measurements for a single sample but the larger differences will remain.

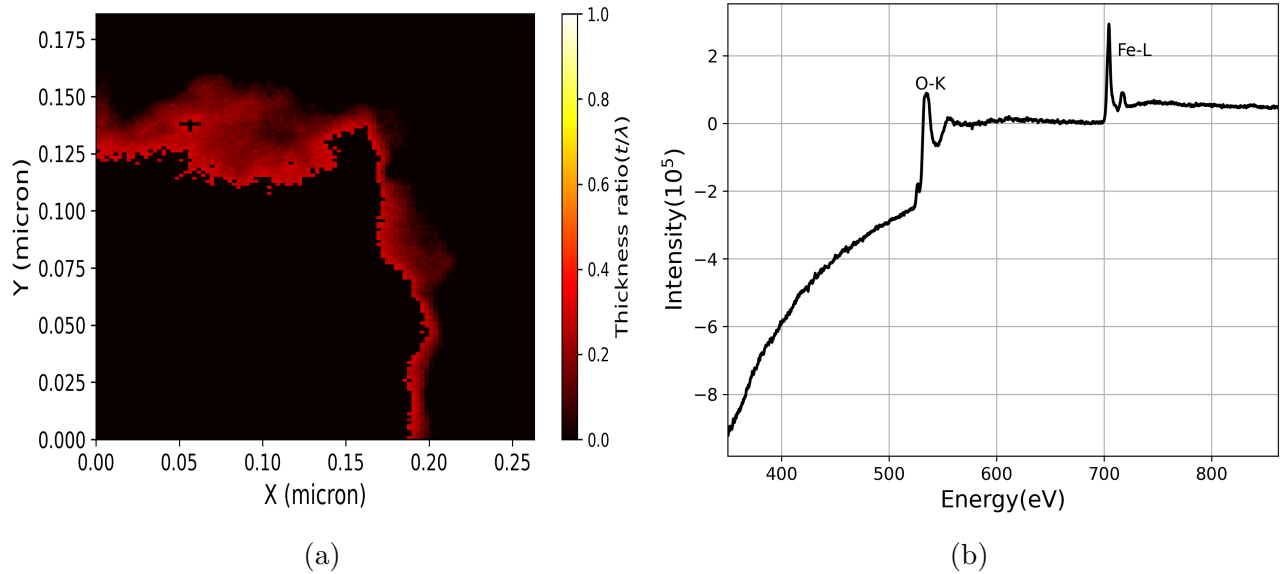


Figure 5: The results after the data processing for a single measurement of the amorphous olivine dust sample. On the left(a) one sees what part of the data is used after the thickness selection where $0 \leq t/\tilde{\lambda} \leq 0.3$. On the right(b) one sees the resulting intensity or electron count spectrum of the same sample containing the oxygen K-edge and the iron L-edges.

3.1.1 Optical constants

After the initial processing of the raw data we went on to calculate the optical constants for each dust sample based on the transmission spectra. The transmission for each measurement was obtained according to Eq. 3 and these were combined into an average transmission per dust type. In order to be consistent and because the thickness varies we needed to normalize the data with respect to the tabulated values by [Henke et al. \(1993\)](#).

Such an averaged and normalized transmission spectrum can be seen in Fig. 6. The pre-edge(<695 eV) and post-edge(>790 eV) regions were matched with the Henke data. We can clearly see that the averaged transmission follows the Henke transmission very closely which is good. Some extra smoothing was done to remove any noise artefacts. The smoothing was important since the initial intensity spectrum contained a number of noise artefacts as can be seen in Fig. 5b. The smoothing was done only for the pre-edge and post-edge energy range to make sure that we did not lose any important data on the edges.

3 RESULTS & DISCUSSION

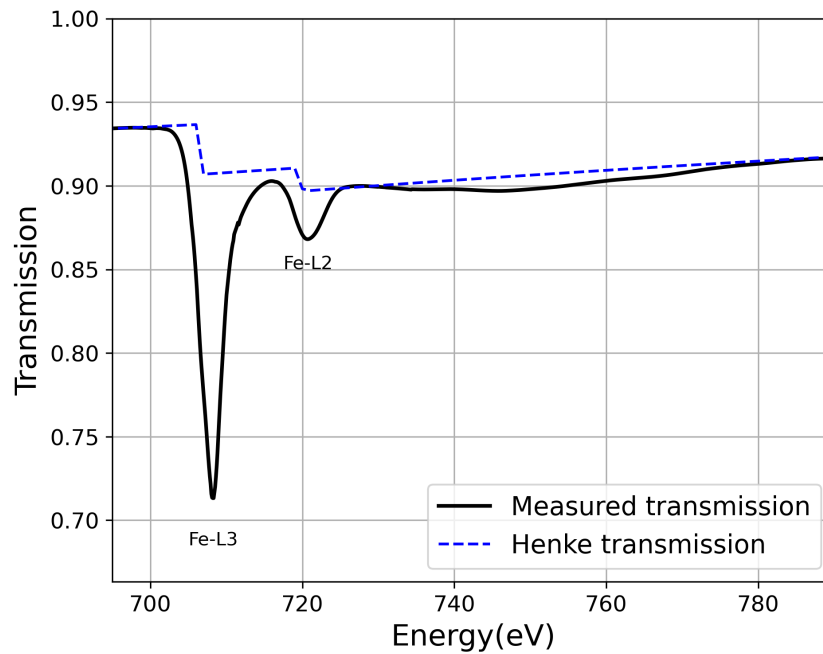


Figure 6: The averaged transmission for amorphous olivine (black) compared to the tabulated Henke transmission (blue) by [Henke et al. \(1993\)](#).

Now that we obtained the averaged transmission for each sample we could use Eq. 3 and 5 to calculate the optical constant k . This k was used to calculate the imaginary part of the atomic scattering factor, f_2 , for each sample using the data from Table 1 and Eq. 8. Now f_2 could be used in the *kkcalc* package to calculate the real part of the atomic scattering factor using Eq. 9.

With Eq. 8 we determined n to obtain the optical constants for each dust type. An example of the resulting optical constants for amorphous olivine can be seen in Fig. 7. Here the imaginary part of the refractive index really resembles the transmission spectrum which was to be expected if one looks at Eq. 5. We also see that k is almost equal to 0 over the entire energy range so there is no strong absorption of the X-rays. The real part of the refractive index had a quite different shape which is not that obvious. However, we do see that n is very close to unity which means that there is hardly any refraction of the incident X-rays. We had already assumed this when we used the Lambert-Beer law earlier and this was indeed a valid assumption.

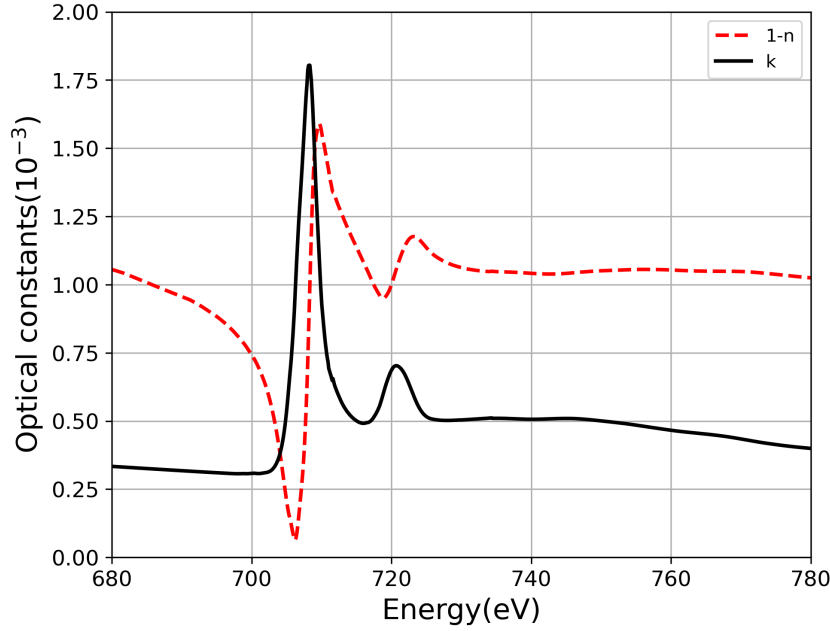


Figure 7: *The calculated optical constants for amorphous olivine by using the averaged transmission. Both the real(red) and imaginary part(black) are plotted.*

3.1.2 Atomic cross sections

Finally, we used the calculated atomic scattering factors to calculate the extinction, absorption and scattering cross section for all samples. For this, we used Eq. 11-14 and the regular MRN grain size distribution. The results for amorphous olivine can be seen in Fig. 8a where the extinction, absorption and scattering cross sections are plotted. In Fig. 8b one sees the cross sections obtained in an earlier analysis of the same raw data. This earlier analysis was done independently and they are basically the same up to some minor differences in peak heights.

First of all, this confirms that the code and the procedure were correct and could reproduce older calculations. Secondly, the differences in peak strength are probably caused by the uncertainties that are introduced during the data analysis. The differences are very small so there are no major flaws but it is almost impossible to reproduce the exact same results.

The results of the ADT calculations for the other samples can be found in Appendix A. We compared these results to the ones obtained in the earlier analysis and could confirm that these give the same results in most cases. The measured extinction profiles are all rather smooth and we cannot directly see any difference between crystalline and amorphous samples.

The pyrite and En60Fs40 dust samples had only a few good data sets with a SNR that was high enough. The lack of data then enlarged minor differences and uncertainties such that the resulting cross sections differed substantially for each analysis. For these three samples our extinction cross sections were all substantially larger than in the earlier analysis. We can conclude that the data for these dust types does not result in very reliable cross section models for the iron L-edges.

Not all differences were caused by the lack of data. These exceptions were fayalite and amorphous En90Fs10. There was a mistake in the code that was used initially such that the peak strength of the iron L-edges for fayalite was much less than it should be. This was corrected in our analysis. For amorphous En90Fs10 it is not completely clear where the difference comes

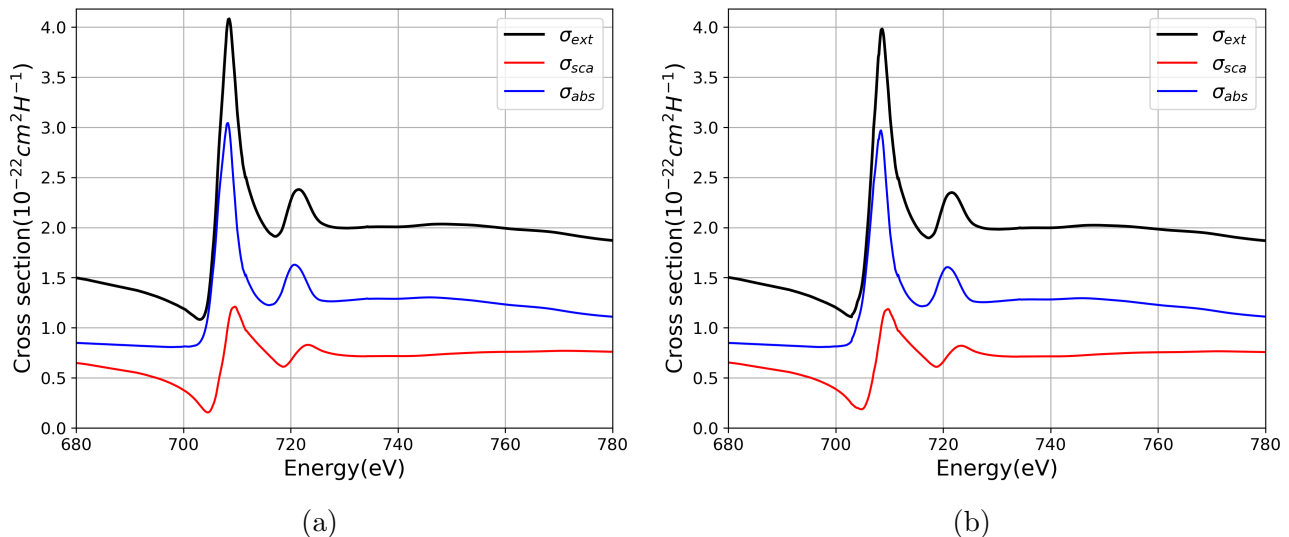


Figure 8: The extinction(black), absorption(blue) and scattering(red) cross sections per hydrogen nucleus of amorphous olivine for the MRN grain size distribution. On the left(a) one sees the calculated cross sections by us and on the right(b) one sees the calculated cross sections from an earlier independent analysis.

from. Perhaps something went wrong with the initial analysis or with the current analysis. However, since crystalline En90Fs10 is almost exactly the same for both analyses we expect that it has something to do with a mistake in the initial analysis.

Ideally, one would like to make use of the EXELFS signal to probe the chemical environment of the iron atoms in the dust samples. However, if we look at Fig. 8a and Appendix A we see that the oscillations in the post-edge region are very weak or even absent for some dust types. The SNR was simply not large enough because we had to discard a lot of data in the thickness selection. This makes it impossible to say anything about the chemical environment of the Fe atoms based on these calculations.

3.2 Large grain size distribution

Now that we are sure that the calculated atomic scattering factors for each dust sample produce smooth extinction cross sections we used a different form of the grain size distribution. The equations for the power law and the ADT calculations remained the same but the difference was that the grain radius interval was enlarged to $0.05 \leq a \leq 0.50 \mu\text{m}$. An example of the resulting extinction, absorption and scattering cross sections for amorphous olivine can be seen in Fig. 9b. Here we can compare the MRN grain size distribution(Fig. 9a) to the larger grain size distribution. The main difference was that the cross sections seem to be somewhat compressed and lie closer together. There seem to be no new features but the scattering cross section does become more important. The results for the extinction cross sections of the other samples can be found in Appendix B and also here we saw the same changes.

We see for some dust types that the extinction cross section becomes stronger and for some it becomes weaker in the large grain size distribution. At first, one would expect the extinction cross section to increase because the dust grains become larger and have a larger surface area. However, it turns out that the density and the crystalline structure of the dust grains also influence the extinction cross section. This means that a larger grain does not necessarily lead to a stronger extinction.

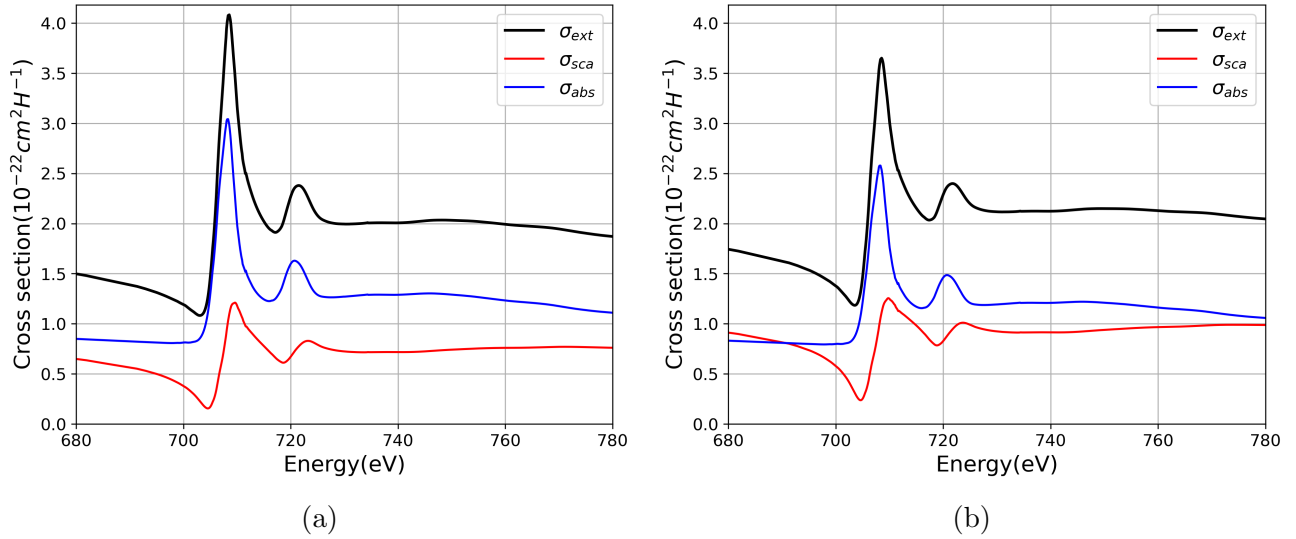


Figure 9: The extinction(black), absorption(blue) and scattering(red) cross sections per hydrogen nucleus of amorphous olivine for both the MRN grain size distribution(a) and the large grain size distribution(b).

3.2.1 Absorption and scattering

In order to gain more insight into the behaviour of the larger dust grains compared to the regular MRN size distribution we can look at the amount of scattering and absorption for each dust type. In Fig. 10 one can see the ratio $\sigma_{abs}/\sigma_{sca}$ for amorphous olivine in both size distributions. The ratio for the other dust types can be found in Appendix C. It is clear that both distributions produce the same overall shape of the ratio which confirms that there are no new features. One can also see that the absorption edges are really dominated by absorption and not scattering as one would expect when n is almost equal to 1.

However, we do see that the absorption efficiency becomes weaker for the large grain size distribution, especially around the L3- and L2-edge. In Fig. 9 it is also clear that the absorption cross section decreases for the large grain size distribution. The scattering cross section becomes somewhat larger and this explains the decrease of $\sigma_{abs}/\sigma_{sca}$. This means that the extinction cross section in the large grain size distribution is still dominated by absorption ($\sigma_{abs}/\sigma_{sca} > 1$) but the scattering component does become stronger.

The only exceptions are En90Fs10 where the scattering component does become dominant ($\sigma_{abs}/\sigma_{sca} < 1$). For other dust types there were only some parts of the graph where the scattering becomes dominant. These parts are also reflected in the graphs in Appendix B. Here the extinction cross section becomes larger for the large grain size distribution for some dust types instead of weaker. These regions correspond with the parts where the scattering component becomes dominant for these dust types.

This result was to be expected if one looks at Eq. 11 where an increase in the grain size or thickness(x) will lead to a decrease in absorption efficiency due to the exponential behaviour. However, it is not that obvious that the scattering becomes equal to the absorption or even dominates. This really depends on the dust type. Initially, one would say that large grains will have a weaker scattering component but this does not apply to the grain sizes we are looking at. In this regime where a is far larger than the wavelength, the scattering becomes stronger relative to the absorption.

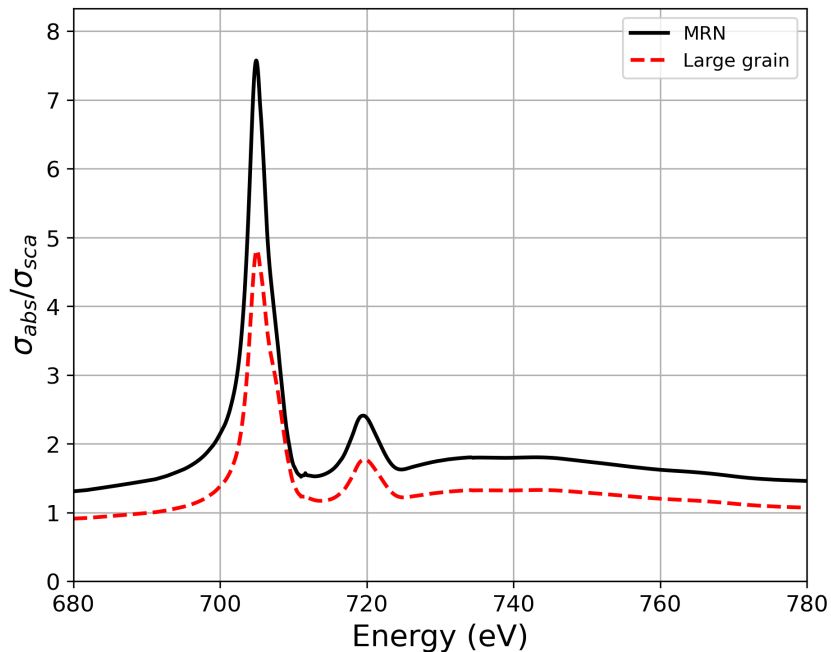


Figure 10: *The ratio of the absorption and scattering cross section for amorphous olivine. The black line represents the ratio for the MRN size distribution and the red dotted line represents the ratio for the large grain size distribution.*

3.2.2 Grain size distributions

We also calculated the normalization constant of each dust type for both grain size distributions to see the difference. These results can be found in Appendix D. We see for both grain size distributions that the normalization constant is around -25 for all samples. Those for the large grain size distribution are a bit more negative. This was to be expected since extending the grain radius interval will lead to a different distribution of dust sizes. In the end, there is a fixed number of dust grains and we cannot create more so it has to spread out, i.e. have a more negative normalization constant.

A comparison plot of the two different size distributions for amorphous olivine can be found in Fig. 11. Note that the grain size distribution is only defined within the grain radius interval. Therefore, we cannot simply extrapolate the MRN size distribution to fit the entire range of $0.05 \leq a \leq 0.50 \mu\text{m}$ in Fig. 11. We do see that both grain size distribution show the same behaviour and lie very close together. Fig. 11 also shows that we can indeed neglect the grains larger than $0.5 \mu\text{m}$. The exponential behaviour of the grain size distributions leads to a very small number of large grains. This also explains why the extinction cross sections in Fig. 9 and Appendix C did not change that much.

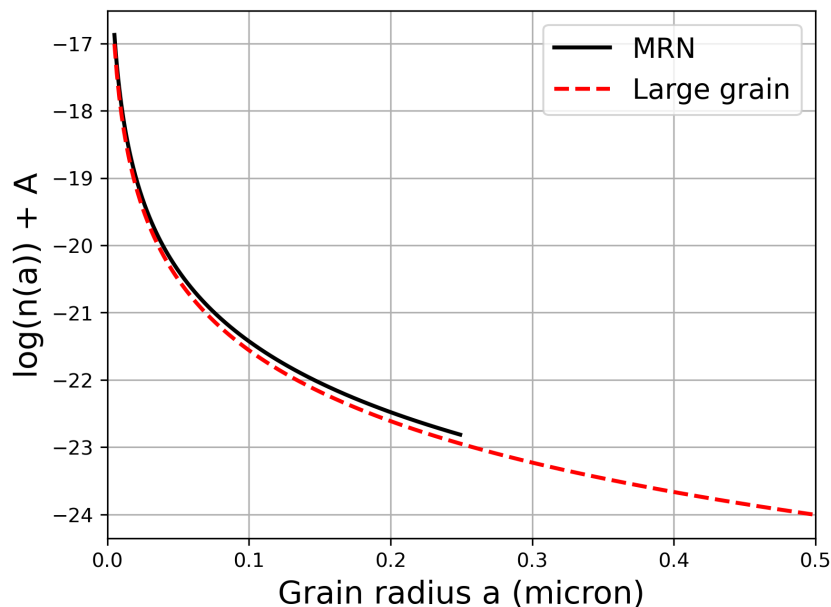


Figure 11: The calculated grain size distributions for amorphous olivine. The result for the MRN distribution is shown in black and the result of the large grain size distribution in red.

3.3 Application to astronomical data

Now that we obtained the extinction cross sections we can implement these into the AMOL model in SPEX. For this, the extinction cross sections need to be converted to the SPEX format as described in Section 2.4. The extinction cross section that was used for amorphous olivine can be seen in Fig. 12. Similar extinction cross sections were obtained for the other dust types. The most important features are that the model starts at zero and has no overall slope which is indeed the case. Furthermore, we can still clearly see the iron L-edges and some post-edge signal.

With these extinction cross sections we can start fitting astronomical data. Such a fit using amorphous olivine can be seen in Fig. 13 where we included data of both the RGS spectrometer of XMM-*Newton* and simulated data of the future X-ray mission *Athena*. Note that the counts on the y-axis refers to the number of X-ray photons that are counted by the detector. *Athena* will have improved spectral resolution and sensitivity, and a larger effective area with respect to current instruments and this is clearly visible in the data.

In order to mimic the ISM we simulated data of a bright background source of which the emitted X-rays travel through clouds of gas and dust before reaching our detectors. Along a typical line of sight these clouds have different temperatures ranging from 90 K up to $8 \cdot 10^5$ K. The lines in the top of Fig. 13 represent the absorption of these different collisionally ionized gases. Depending on the chemistry and temperature of the medium these absorb at characteristic energies which gives rise to certain dips in the lines.

The green line in Fig. 13 represents the absorption of amorphous olivine as modeled by the extinction cross section we presented in Fig. 12. One clearly sees the iron L-edges which are also indicated and these match the real astronomical data of XMM-*Newton* quite nicely. This confirms that the models that we found are sufficient to explain current astronomical data and can give us insight into the amount of iron in the ISM. However, we do see that the L2-edge is rather unclear in the current data which is not good enough to resolve different dust types. The

future data of *Athena* has a much higher resolution and it matches the extinction model much better. This will allow us to identify the dust in the ISM more precisely.

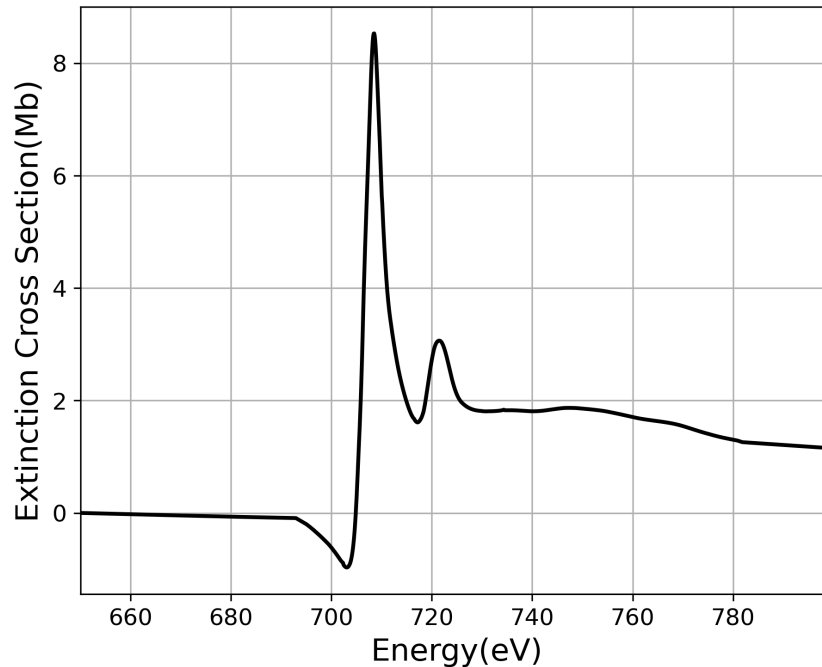


Figure 12: *The extinction cross section for amorphous olivine in Mb per Fe nucleus as used in SPEX.*

In Fig. 13 we only show the absorption of collisionally ionized gases and the extinction cross section of amorphous olivine compared to astronomical data. In principal, one can also add more gas and dust components to see how this fits the data using some statistical criterion like χ^2 -statistics. By testing combinations of different dust types one can find the best fit and ultimately find the chemical composition of the ISM. However, there will always be differences between different lines of sight and different galactic environments so a map of the ISM still requires some work.

In the end, we can conclude that the SNR and the resolution (0.25 eV) of the extinction models allowed us to resolve the iron L-edges for several interstellar dust analogues. These models for both grain size intervals are sufficient to fit the astronomical data since their uncertainties fall within the limit of precision of currently used telescopes. For the future, it is important to improve laboratory models to keep up with the improvement of astronomical data from future missions like *Athena*. In this way, we can also investigate the EXELFS signal to get a more complete picture of the chemical composition of the ISM. On top of that, it is just as important to create an even larger set of interstellar dust analogues until the astronomical data can be explained.

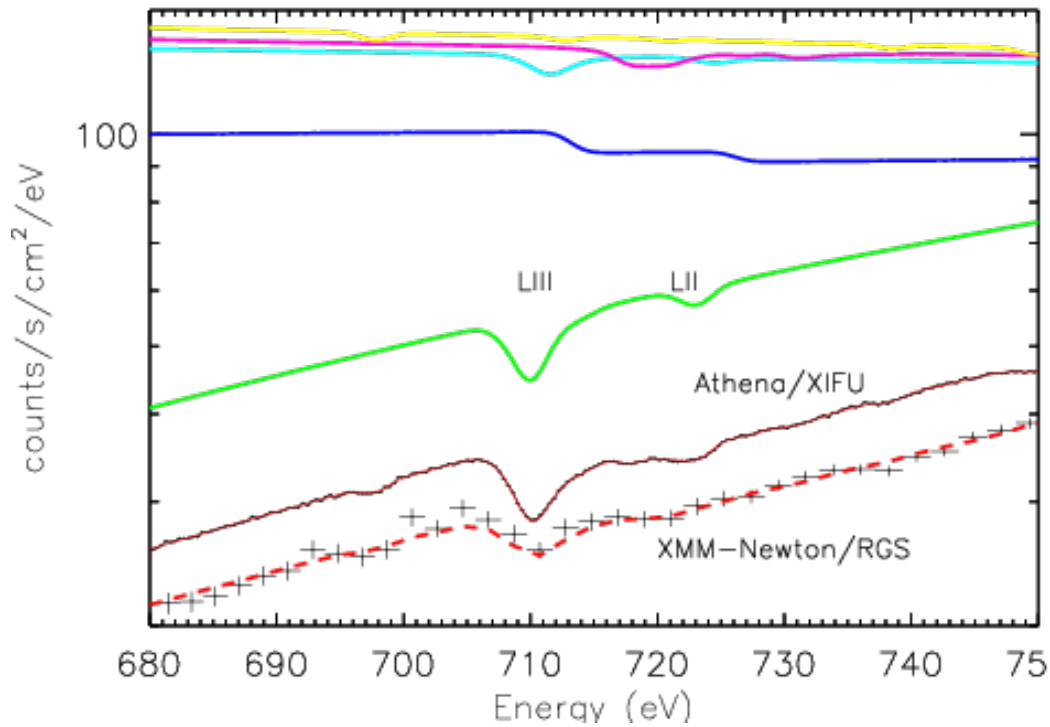


Figure 13: *Simulation of the absorption by a multitemperature cloud of gas and dust in our Galaxy of the spectrum of a bright background source. The solid red line and associated data belong to the future X-ray mission Athena. The dashed red line and associated data belong to the currently in operation RGS spectrometer, on board of XMM-Newton. The green line indicates absorption by amorphous olivine dust, while the other colors indicate collisionally ionized gas with different temperatures, as observed for a typical sight line of the Milky Way. These temperatures range from 90 K (blue line) up to $8 \cdot 10^5$ K (yellow line).*

4 Conclusions & Outlook

In this thesis we calculated the extinction cross section around the iron L-edges of 14 interstellar dust analogues. We used EELS measurements to obtain laboratory transmission data which is the same as X-ray absorption data under the dipole approximation. This transmission data was related to the optical constants of each material which were used to calculate extinction cross sections based on the MRN grain size distribution. Furthermore, we looked at the effect of increasing the grain size window of the MRN distribution on the extinction cross sections. Lastly, we implemented the extinction model of amorphous olivine into SPEX to fit astronomical data of the current *XMM-Newton* mission and the future *Athena* mission.

This resulted in extinction cross sections with a resolution and SNR that were good enough to fit present and future astronomical data. However, the SNR did not allow for an analysis of the EXELFS to look at the chemical environment of the iron atoms. The larger grain size distribution resulted in very similar extinction cross sections except that they seemed to be somewhat compressed and had a relatively stronger scattering component. Lastly, we looked at a simulated astrophysical spectrum of the future *Athena* mission compared to data of the *XMM-Newton* mission using the obtained extinction models. This confirmed that our models are sufficient to explain current and future astronomical data.

In the past years, a lot of interstellar dust analogues and their absorption edges have been investigated (see for example [Zeegers et al. \(2017\)](#), [Rogantini et al. \(2018\)](#), [Psaradaki et al. \(2020\)](#)). For the future, it is important to do EELS measurements with a higher resolution such that the extinction models become more accurate. Better models can be used to find possible instrumental artifacts and allow for a more precise analysis of astronomical data. If more is known about the chemical composition one could even try to recreate the interstellar dust grains. In this way one can verify the dust composition of the interstellar medium even better.

On the other hand, it is just as important to improve the resolution of the X-ray missions that acquire the astronomical data. There are definitely some promising developments for future missions such as *Athena* and *XRISM* which can do this. These have a better resolving power than current missions and can help explain any unidentified features in current observations and rule out any instrumental artefacts [[Rogantini et al. \(2019\)](#)]. The goal of mapping the complete chemical composition of the ISM has not yet been achieved but with current developments we are coming closer and closer to this goal.

Acknowledgements

While I was working on my thesis a lot of people helped and supported me, and I would like to thank them. First of all, there is my supervisor, Dr. Elisa Costantini from SRON, who guided me through all the new concepts in this field of research and was always willing to help with my questions. She offered me the opportunity to do my first research and gave me a lot of freedom for which I am grateful.

I would also like to thank Prof. Dr. Frank de Groot and Dr. Laura Fillion for being my supervisors from the University of Utrecht. Even though they were not my daily supervisors they were always willing to answer my questions and gave me very useful advice.

Lastly, I want to thank B. Watts for helping me out with understanding the functions in the kkcalt package when it turned out that the graphical interface of the kkcalt package did not work anymore. With his help and the kkcalt package itself we could do this analysis.

References

- J. S. Mathis, *The Astrophysical Journal* **472**, 643 (1996).
- J. P. Bradley, *Science* **265**, 925 (1994).
- B. T. Draine, *Annual Review of Astronomy and Astrophysics* **41**, 241 (2003).
- D. Whittet, *Dust in the galactic environment, second edition* (2002).
- E. Costantini and C. P. de Vries, *Mem. Societa Astronomica Italiana* **84**, 592 (2013).
- L. Corrales, L. Valencic, E. Costantini, J. Garcia, E. Gatuzz, T. Kallman, J. Lee, N. Schulz, S. Zeegers, C. Canizares, et al., *Bulletin of the American Astronomical Society* **51**, 264 (2019).
- R. Egerton, *Electron Energy-Loss Spectroscopy in the Electron Microscope, 3rd Edition* (Springer, 2011).
- P. S. Miedema and F. M. de Groot, *Journal of Electron Spectroscopy and Related Phenomena* **187**, 32 (2013), ISSN 0368-2048.
- S. T. Zeegers, E. Costantini, C. P. de Vries, A. G. G. M. Tielens, H. Chihara, F. de Groot, H. Mutschke, L. B. F. M. Waters, and S. Zeidler, *A&A* **599**, A117 (2017).
- J. S. Kaastra, R. Mewe, and H. Nieuwenhuijzen, in *UV and X-ray Spectroscopy of Astrophysical and Laboratory Plasmas* (1996), pp. 411–414.
- D. Rogantini, E. Costantini, S. T. Zeegers, C. P. de Vries, W. Bras, F. de Groot, H. Mutschke, and L. B. F. M. Waters, *A&A* **609**, A22 (2018).
- I. Psaradaki, E. Costantini, M. Mehdipour, D. Rogantini, C. P. de Vries, F. de Groot, H. Mutschke, S. Trasobares, L. B. F. M. Waters, and S. T. Zeegers, *A&A* **642**, A208 (2020).
- D. Coster and R. de L. Kronig, *Physica* **2**, 13 (1935), ISSN 0031-8914.
- F. M. de Groot, H. Elnaggar, F. Frati, R. pan Wang, M. U. Delgado-Jaime, M. van Veenendaal, J. Fernandez-Rodriguez, M. W. Haverkort, R. J. Green, G. van der Laan, et al., *Journal of Electron Spectroscopy and Related Phenomena* **249**, 147061 (2021), ISSN 0368-2048.
- J. Jasinski, K. E. Pinkerton, I. Kennedy, and V. J. Leppert, *Microscopy and Microanalysis* **12**, 424–431 (2006).
- J. C. Fuggle and N. Mårtensson, *Journal of Electron Spectroscopy and Related Phenomena* **21**, 275 (1980), ISSN 0368-2048.
- D. A. Verner, G. J. Ferland, K. T. Korista, and D. G. Yakovlev, *The Astrophysical Journal* **465**, 487 (1996).
- C. Colliex, T. Manoubi, and C. Ortiz, *Phys. Rev. B* **44**, 11402 (1991).
- M. Min, L. B. F. M. Waters, A. de Koter, J. W. Hovenier, L. P. Keller, and F. Markwick-Kemper, *American Academy of Pediatrics* **462**, 667 (2007).
- A. P. Jones and J. A. Nuth, *American Academy of Pediatrics* **530**, A44 (2011).
- D. Rogantini, E. Costantini, S. T. Zeegers, C. P. de Vries, M. Mehdipour, F. de Groot, H. Mutschke, I. Psaradaki, and L. B. F. M. Waters, *Astronomy & Astrophysics* **630**, A143 (2019).
- S. Zeegers, E. Costantini, D. Rogantini, C. Vries, H. Mutschke, P. Mohr, F. Groot, and A. Tielens, *Astronomy & Astrophysics* **627** (2019).
- J. B. Kortright and S.-K. Kim, *Phys. Rev. B* **62**, 12216 (2000).
- R. Manzorro, W. E. Celín, J. A. Pérez-Omil, J. J. Calvino, and S. Trasobares, *ACS Catalysis* **9**, 5157 (2019).
- L. G. Parratt, C. F. Hempstead, and E. L. Jossem, *Phys. Rev.* **105**, 1228 (1957).
- G. Bunker, *Introduction to XAFS: A Practical Guide to X-ray Absorption Fine Structure Spectroscopy* (Cambridge University Press, 2010).
- N. Jiang and J. Spence, *Ultramicroscopy* **106**, 215 (2006), ISSN 0304-3991.

- L. A. J. Garvie, *American Mineralogist* **95**, 92 (2010).
- K. F. Pearson, *The London, Edinburgh, and Dublin Philosophical Magazine and Journal of Science* **2**, 559 (1901).
- B. L. Henke, E. M. Gullikson, and J. C. Davis, *Atomic Data and Nuclear Data Tables* **54**, 181 (1993).
- C. F. Bohren, *European Journal of Physics* **31**, 573 (2010).
- A. Thompson, D. Attwood, E. Gullikson, M. Howells, K.-J. Kim, J. Kirz, J. Kortright, I. Lindau, P. Pianetta, A. Robinson, et al., University of California, Berkeley, CA **94720** (2001).
- L. D. Landau and E. M. Lifshitz, *Electrodynamics of continuous media*, Their Course of theoretical physics, v. 8 (Pergamon Press, Oxford, 1960).
- B. Watts, *Optics Express* **22**, 23628 (2014).
- G. Mie, *Annalen der Physik* **330**, 377 (1908).
- H. van de Hulst, *Quarterly Journal of the Royal Meteorological Society* **84**, 198 (1958).
- J. Hoffman and B. T. Draine, *The Astrophysical Journal* **817**, 139 (2016).
- J. S. Mathis, W. Rumpl, and K. H. Nordsieck, *The Astrophysical Journal* **217**, 425 (1977).
- C. W. Mauche and P. Gorenstein, *The Astrophysical Journal* **302**, 371 (1986).
- J. S. Kaastra, A. J. J. Raassen, J. de Plaa, and L. Gu, *Spex x-ray spectral fitting package* (2020).
- K. Lodders, H. Palme, and H.-P. Gail, in *Solar System* (Springer Berlin Heidelberg, 2009), pp. 712–770.
- K. Nandra, D. Barret, X. Barcons, A. Fabian, J.-W. d. Herder, L. Piro, M. Watson, C. Adami, J. Aird, J. M. Afonso, et al., *The hot and energetic universe: A white paper presenting the science theme motivating the athena+ mission* (2013).
- D. Barret, T. L. Trong, J.-W. den Herder, L. Piro, X. Barcons, J. Huovelin, R. Kelley, J. M. Mas-Hesse, K. Mitsuda, S. Paltani, et al., in *SPIE Proceedings*, edited by J.-W. A. den Herder, T. Takahashi, and M. Bautz (SPIE, 2016).

Appendix A Extinction, scattering and absorption cross sections

In Fig. A.1 we show the calculated extinction, scattering and absorption cross section for all dust samples in Table 1, except amorphous olivine, based on the MRN grain size distribution. This data was obtained using the STEM facility at the University of Cadiz and the cross sections were obtained as was described in Section 2.

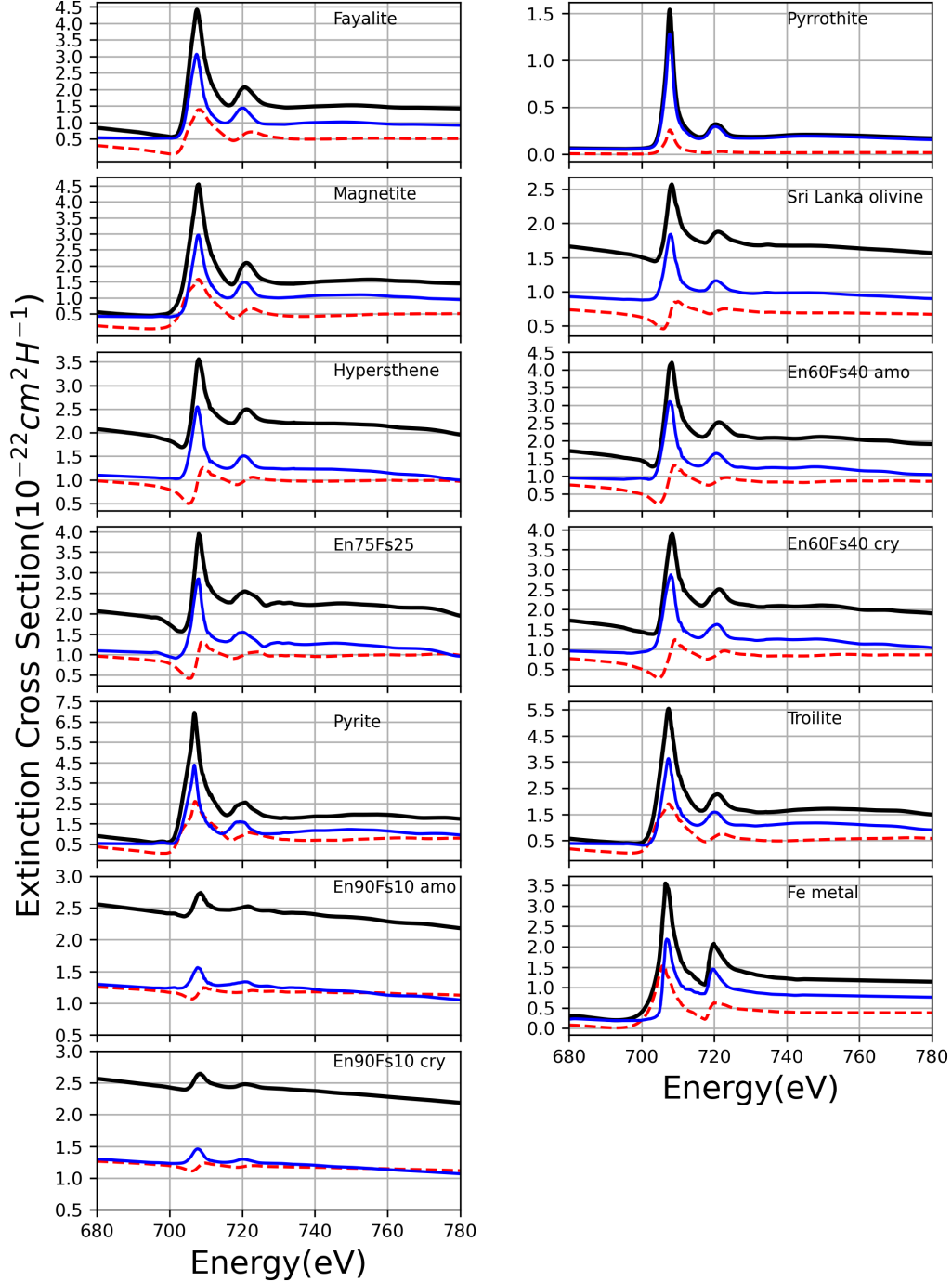


Figure A.1: The extinction, scattering and absorption cross sections for all samples except amorphous olivine. The calculated extinction, scattering and absorption cross sections are given by the black, red and blue line, respectively.

Appendix B Extinction for both grain size distributions

In Fig. B.1 we present the extinction cross section of all samples in Table 1, except amorphous olivine, around the iron L-edges for both grain size distributions. This data was obtained using the STEM facility at the University of Cadiz and the cross sections were obtained as was described in Section 2.

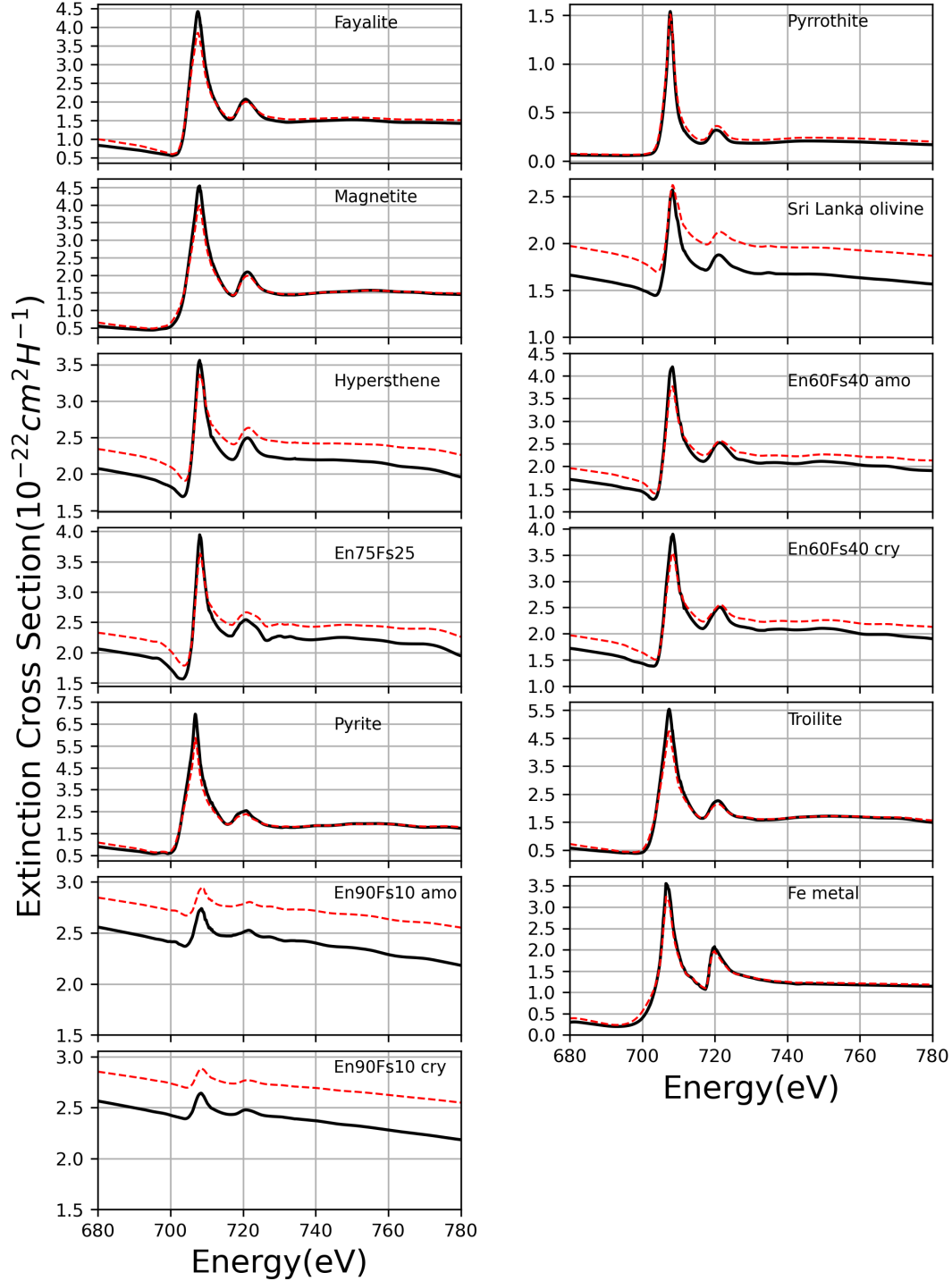


Figure B.1: *The extinction cross sections for all samples except amorphous olivine. The black line is the extinction cross section for the MRN grain size distribution and the red broken line is the extinction cross section for the large grain size distribution.*

Appendix C The ratio of absorption and scattering

In Fig. C.1 we present the ratio of the absorption and scattering cross section of all samples in Table 1 around the iron L-edges for both grain size distributions. This data was obtained using the STEM facility at the University of Cadiz and the cross sections were obtained as was described in Section 2.

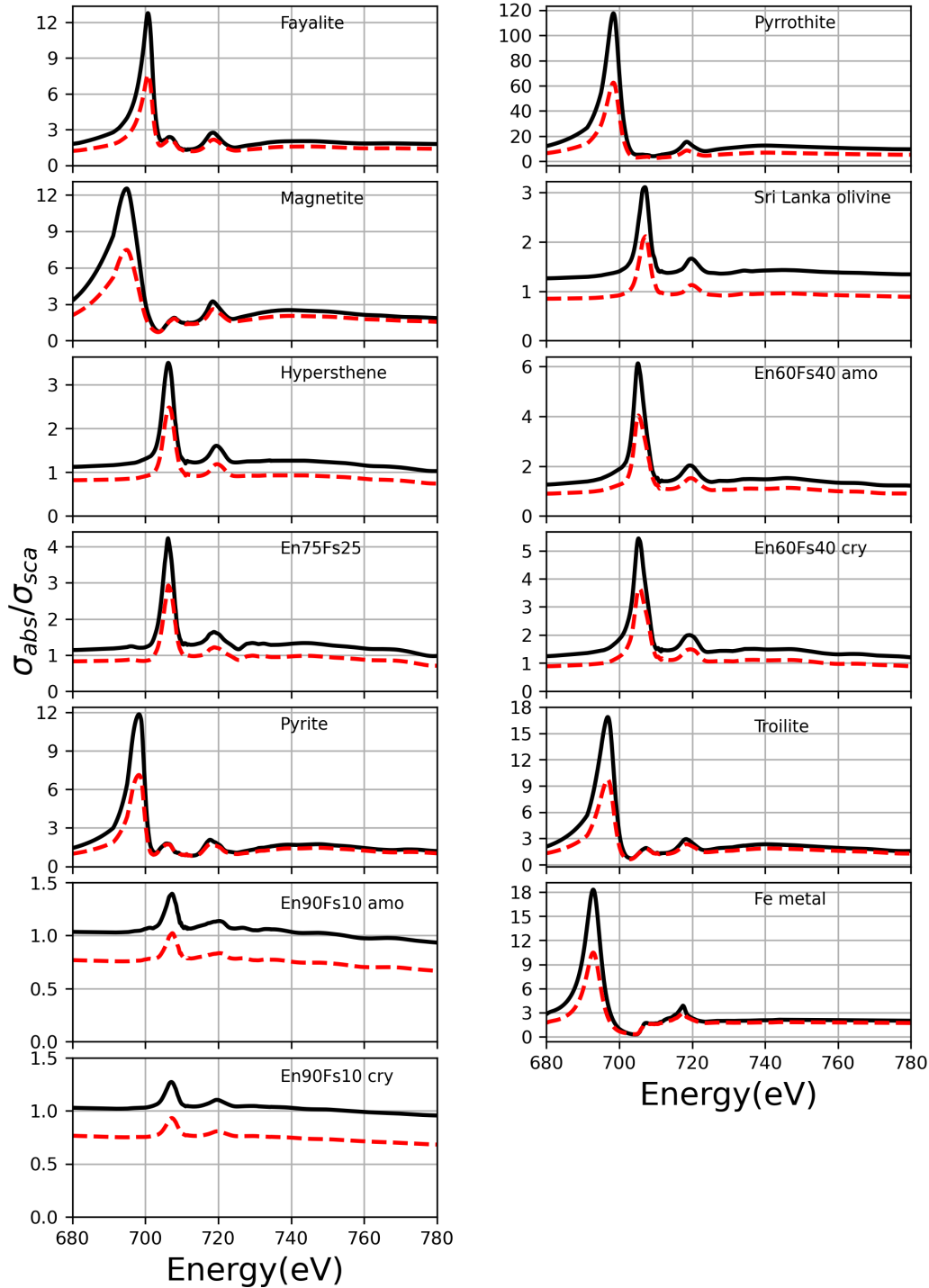


Figure C.1: The ratio of the absorption and scattering cross sections of all samples. The black line is the ratio for the MRN grain size distribution and the red broken line is the ratio for the large grain size distribution.

Appendix D Normalization constants

In Table D.1 we present the results of the calculated normalization constants of each dust type for both grain size distributions. For this, we used the calculated optical constants n and k at an energy of 1 keV and the grain size distributions as described in Section 2.

Note that for some samples the normalization constant is exactly the same. This is caused by the fact that we used a crystalline and an amorphous type of that mineral which has the same density and molecular mass. If one looks at Eq. 8 then one sees that the crystallinity does not affect n and k so the input for the calculation of A_i is the same.

Sample name	MRN distribution	Large grain distribution
Fayalite ^(c)	-25.160430	-25.272817
Magnetite ^(c)	-25.276692	-25.376143
Hyperstene ^(a)	-24.839054	-24.978092
En75Fs25 ^(c)	-24.839413	-24.978428
Olivine ^(a)	-24.926319	-25.059455
Olivine ^(c)	-24.815633	-24.956101
En90Fs10 ^(a)	-24.767403	-24.910621
En90Fs10 ^(c)	-24.767403	-24.910621
En60Fs40 ^(a)	-24.896994	-25.032218
En60Fs40 ^(c)	-24.896994	-25.032218
Pyrrhotite ^(c)	-25.167775	-25.279392
Pyrite ^(c)	-25.144882	-25.258876
Troilite ^(c)	-25.183412	-25.293368
Metallic iron ^(c)	-25.449181	-25.527379

Table D.1: The normalization constants of all dust samples for both grain size distributions in units of $\text{cm}^{2.5}$. The sample names are labeled as ^(a)Amorphous samples and ^(c)Crystalline samples.